Variational integrators for soundproof models on arbitrary triangular C-grids

Werner Bauer, François Gay-Balmaz

Variational integrators for soundproof models on arbitrary triangular C-grids

Werner Bauer[1,2] and François Gay-Balmaz[2]

Abstract

We introduce variational integrators for soundproof approximations of the Euler equations on irregular triangular C-grids. In particular we provide explicit vector-matrix formulations and the solving algorithm for the previously derived discrete covariant equations of Boussinesq, anelastic, and pseudo-incompressible models of [4]. The derivation of these variational integrators is based on a discrete version of the Euler-Poincaré variational method, hence it provides structure-preserving discretizations that preserve Kelvin's circulation theorem and provide excellent long term energy behavior for arbitrary triangular C-grids. We verify the structure-preserving nature of these schemes for various scenarios of geophysical relevance: the hydrostatic adjustment process, the Kelvin-Helmholtz instability, and the cold and warm bubble test cases.

1 Introduction

Reliable numerical simulations of the dynamics of the atmosphere require accurate and efficient computation models that well represent long-terms features such as correct statistical mean or the preservation of the structure of the underlying fluid equations, expressed in the conservation of mass, energy, and enstrophy, for instance. Treating highly multiscale phenomena, high resolution is required on the global scale to capture important small scale features, such as the process of cloud condensation in global atmosphere models. However, with higher resolution the time step size gets smaller for explicit time integration schemes leading to much more computation cost.

When considering the full Euler equations, this restriction of the time step size (denoted as CFL number) is determined by the fast traveling sound waves which have to be fully resolved to guarantee the stability of the numerical scheme [10]. However, sound waves are assumed to be negligible in atmospheric flows. An option to increase computational efficiency is to used equations of motions in which the sound waves have been filtered out. These approximations of the full Euler equations are usually referred to as soundproof models. Frequently applied soundproof models are the Boussinesq, anelastic, and pseudo-incompressible approximations of the full Euler equations [9, 22, 25].

To guarantee accurate simulations that preserve the geometric properties of the underlying differential equations (e.g. symplectic and volume forms, Lie symmetries, conservation laws,

[1]Imperial College London, Department of Mathematics. werner.bauer@lmd.ens.fr

[2]CNRS/École Normale Supérieure, Laboratoire de Météorologie Dynamique, Paris, France. gaybalma@lmd.ens.fr

variational formulations), a viable option is to use geometric numerical integrators that discretely preserve some of these geometrical structures, cf. [4, 3, 5, 6, 16, 19, 24, 26, 27, 28]. Schemes that are capable of preserving these geometrical properties usually show improved long-term behavior, such as long-term stability or a consistent representation of statistical properties, see e.g. [16, 19, 29].

Recently, these geometrical methods have been developed for partial differential equations of fluids and the equations of geophysical fluid dynamics (GFD) [26, 12, 7]. These structure-preserving schemes descend from the Euler-Poincaré variational principle. They conserve quantities such as mass, momentum, energy, or guarantee that the Helmholtz decomposition of vector fields or the Kelvin-Noether circulation theorem hold. This follows as the discrete equations descend from a Lagrangian formulation, in which these conserved quantities follow from Noether's theorem as they are invariants of the Lagrangian under symmetries, cf. [15].

In [4] we developed such variational integrators based on a discrete version of the Euler-Poincaré variational principle for soundproof models. Although there exists elaborated discretizations of these approximations in literature, usually the corresponding schemes are not fully structure-preserving. We included the anelastic and pseudo-incompressible schemes into the variational discretization framework developed by [26] and we derived for all three approximations structure-preserving integrators on unstructured 2D simplicial meshes. By introducing Lie groups of diffeomorphisms that preserve volume forms that are weighted by the background stratification, the corresponding Lie algebras provided weighted velocity fields that preserve the corresponding divergence-free conditions associated to the different soundproof models. Using the velocity fields to define appropriate discrete Lagrangians, the discrete equations of motion followed by Hamilton's variational principle of stationary action.

In this contribution, we address the GFD community by providing explicit vector-matrix formulations of the Boussinesq, anelastic, and pseudo-incompressible variational integrators on unstructured staggered triangular C-grids that were originally derived in the aforementioned manuscript [4] in term of discrete covariant equations. In addition, we explicitly present the time discretization and the solving algorithm. Besides a presentation of the schemes in a more conventional form, the major contribution of this paper consists in an exhaustive study of the variational integrators for soundproof models for scenarios of geophysical relevance. This suit of test cases covers the study of the schemes' wave representation for the hydrostatic adjustment process, their representation of nonlinear effect for the rising or falling bubble test cases, and whether the schemes are able to correctly capture the stability threshold with respect to the Kelvin-Helmholtz instability.

This paper is structured as follows. In Section 2 we recall shortly the continuous Euler-Poincaré theory for soundproof models (i.e. for Boussinesq, anelastic, and pseudo-incompressible approximations of the Euler equations for perfect fluids), as developed in [4]. In Section 3 we present a summary of the variational discretization framework for these soundproof models. In Section 4 we recall the corresponding discretizations on triangular C-grids while providing explicit formulations in terms of velocity and buoyancy, respectively, potential temperature fields. In Section 5 we perform numerical tests of geophysical relevance to demonstrate the structure-preserving nature of these variational integrators. In Section 6 we draw conclusions and provide an outlook.

2 Continuous variational theory for soundproof models

Diffeomorphism groups describe the configuration spaces of the soundproof fluid models. Let μ be a volume form on the fluid domain $\mathcal{D}$. The Lie group $\mathrm{Diff}_{\bar{\sigma}\mu}(\mathcal{D})$ consists of all smooth diffeomorphisms $\varphi : \mathcal{D} \to \mathcal{D}$ that preserve the weighted volume form $\bar{\sigma}\mu$, i.e., $\varphi^*\bar{\sigma}\mu = \bar{\sigma}\mu$, in which $\bar{\sigma}(\mathbf{x}) > 0$ is a strictly positive function $\bar{\sigma}(\mathbf{x}) > 0$ on the fluid domain $\mathcal{D}$. Then, the motions of the fluid is fully described by a curve $\varphi_t(\ ) \in \mathrm{Diff}_{\bar{\sigma}\mu}(\mathcal{D})$; a particle at point $X \in \mathcal{D}$ at $t = 0$ evolves to $\mathbf{x} = \varphi_t(X) \in \mathcal{D}$ at time t.

As we shall see further below, the choice of parameter $\bar{\sigma}$ allows us to describe different soundproof approximations of the Euler equations, i.e. we find for

- $\bar{\sigma} = 1$ the Boussinesq (incompressible) model
- $\bar{\sigma} = \bar{\rho}$ the anelastic model, and
- $\bar{\sigma} = \bar{\rho}\bar{\theta}$ the pseudo-incompressible model.

In the following we introduce the variational principles for soundproof models with the general parameter $\bar{\sigma}$.

In contrast to the incompressible Euler equations, in which we only prognose the velocity field, soundproof models depend on an additional parameter, namely the potential temperature (or buoyancy) field. This field, denoted by Θ_0 in the Lagrangian description, is advected by the flow. We denote the material Lagrangian with L_{Θ_0} that depend on the parameter Θ_0. We assume that L_{Θ_0} is right-invariant with respect to the action of the subgroup

$$\mathrm{Diff}_{\bar{\sigma}\mu}(\mathcal{D})_{\Theta_0} = \{\varphi \in \mathrm{Diff}_{\bar{\sigma}\mu}(\mathcal{D}) \mid \Theta_0(\varphi(X)) = \Theta_0(X),\ \forall\, X \in \mathcal{D}\} \tag{2.1}$$

of all diffeomorphisms that keep Θ_0 invariant. In the Lagrangian picture, the equations of motion follow from the Hamilton principle

$$\delta \int_0^T L_{\Theta_0}(\varphi, \dot{\varphi}) dt = 0, \tag{2.2}$$

over a time interval $[0, T]$, for variations $\delta\varphi$ with $\delta\varphi(0) = \delta\varphi(T) = 0$. Here the Lagrangian $L_{\Theta_0} : T\,\mathrm{Diff}_{\bar{\sigma}\mu}(\mathcal{D}) \to \mathbb{R}$ is defined on the tangent bundle $T\,\mathrm{Diff}_{\bar{\sigma}\mu}(\mathcal{D})$, as in classical mechanics, and it depend on the potential temperature Θ_0 that is advected by the flow.

For fluids, we rather use the Eulerian than the Lagrangian description. We use the spacial fields Eulerian velocity $\mathbf{u}(t, \mathbf{x})$ and the potential temperature $\theta(t, \mathbf{x})$. The relation to the Lagrangian variables $\varphi(t, X)$ and $\Theta_0(X)$ is

$$\mathbf{u}(t, \varphi(t, X)) = \dot{\varphi}(t, X) \quad \text{and} \quad \theta(t, \varphi(t, X)) = \Theta_0(X). \tag{2.3}$$

The Eulerian velocity is element of the Lie algebra of the group $\mathrm{Diff}_{\bar{\sigma}\mu}(\mathcal{D})$. It is given by

$$\mathfrak{X}_{\bar{\sigma}\mu}(\mathcal{D}) = \{\mathbf{u} \in \mathfrak{X}(\mathcal{D}) \mid \mathrm{div}_{\bar{\sigma}\mu}(\mathbf{u}) = 0,\ \ \mathbf{u} \parallel \partial\mathcal{D}\},\ \text{or, equivalently,} \tag{2.4}$$

$$\mathfrak{X}_{\bar{\sigma}\mu}(\mathcal{D}) = \{\mathbf{u} \in \mathfrak{X}(\mathcal{D}) \mid \mathrm{div}_{\mu}(\bar{\sigma}\mathbf{u}) = 0,\ \ \mathbf{u} \parallel \partial\mathcal{D}\} \tag{2.5}$$

The condition $\mathrm{div}_{\bar{\sigma}\mu}(\mathbf{u}) = 0$ can be rewritten by using exclusively the divergence operator div_μ associated to the initial volume form μ (cf. [4]).

The right invariance in Θ_0 in (2.1) allows us to reduce L_{Θ_0} to the spatial Lagrangian $\ell(\mathbf{u},\theta)$ that only depends on the spatial (Eulerian) variables $\mathbf{u}$ and θ. Then, in terms of these spatial variables, we get the Euler-Poincaré variational principle

$$\delta\int_0^T \ell(\mathbf{u},\theta)dt = 0, \quad \text{for variations} \quad \delta\mathbf{u} = \partial_t\mathbf{v} + [\mathbf{u},\mathbf{v}], \quad \delta\theta = -\mathbf{d}\theta\cdot\mathbf{v}, \tag{2.6}$$

where $\mathbf{v}(t,\mathbf{x})$ is an arbitrary vector field on $\mathcal{D}$ parallel to the boundary and with $\mathrm{div}_\mu(\bar\sigma\mathbf{v}) = 0$, (i.e., $\mathbf{v}\in\mathfrak{X}_{\bar\sigma\mu}(\mathcal{D})$ by (2.5)), and with $\mathbf{v}(0,\mathbf{x}) = \mathbf{v}(T,\mathbf{x}) = 0$. The bracket $[\mathbf{u},\mathbf{v}]$, locally given by $[\mathbf{u},\mathbf{v}]^i := u^j\partial_j v^i - v^j\partial_j u^i$, is the Lie bracket of vector fields.

The Euler-Poincaré variational principle yields the following Euler-Poincaré equations:

$$\partial_t\frac{\delta\ell}{\delta\mathbf{u}} + \pounds_{\mathbf{u}}\frac{\delta\ell}{\delta\mathbf{u}} + \frac{\delta\ell}{\delta\theta}\mathbf{d}\theta = -\mathbf{d}p, \quad \text{with} \quad \mathrm{div}_\mu(\bar\sigma\mathbf{u}) = 0, \quad \mathbf{u}\,\|\,\partial\mathcal{D}, \tag{2.7}$$

where $\pounds_{\mathbf{u}}$ denotes the Lie derivative acting on one-forms and θ is transported by the advection equation

$$\partial_t\theta + \mathbf{d}\theta\cdot\mathbf{u} = 0.$$

The functional derivatives are computed with respect to the following duality pairings. The continuous nondegenerate duality pairing to identify the dual to the space of functions $\mathcal{F}(\mathcal{D})$ with itself is given by

$$\mathcal{F}(\mathcal{D})\times\mathcal{F}(\mathcal{D})\to\mathbb{R}, \quad \langle h,\theta\rangle_{\bar\sigma} = \int_{\mathcal{D}}(h\theta)\bar\sigma\mu. \tag{2.8}$$

The nondegenerate duality pairing between the space $\Omega^1(\mathcal{D})/\mathbf{d}\Omega^0(\mathcal{D})$ of one-forms modulo exact forms with the space $\mathfrak{X}_{\bar\sigma\mu}(\mathcal{D})$, the Lie algebra of $\mathrm{Diff}_{\bar\sigma\mu}(\mathcal{D})$, is given by

$$\langle\ ,\ \rangle_{\bar\sigma} : \Omega^1(\mathcal{D})/\mathbf{d}\Omega^0(\mathcal{D})\times\mathfrak{X}_{\bar\sigma\mu}(\mathcal{D})\to\mathbb{R}, \quad \langle[\alpha],\mathbf{u}\rangle_{\bar\sigma} := \int_{\mathcal{D}}(\alpha\cdot\mathbf{u})\bar\sigma\mu, \tag{2.9}$$

where $[\alpha]$ denotes the equivalence class of α modulo exact forms.

Given a Lagrangian $\ell : \mathfrak{X}_{\bar\sigma\mu}(\mathcal{D})\times\mathcal{F}(\mathcal{D})\to\mathbb{R}$, the functional derivatives of ℓ are defined with respect to the parings (2.9) and (2.8) and denoted

$$\left[\frac{\delta\ell}{\delta\mathbf{u}}\right]\in\Omega^1(\mathcal{D})/\mathbf{d}\Omega^0(\mathcal{D}), \quad \text{for } \frac{\delta\ell}{\delta\mathbf{u}}\in\Omega^1(\mathcal{D}), \qquad \text{and} \qquad \frac{\delta\ell}{\delta\theta}\in\mathcal{F}(\mathcal{D}).$$

Substituting the functional derivatives for a given Lagrangian in the Euler-Poincaré equations gives the equations of motion.

We illustrate this shortly for the three schemes discuss here. We discuss 2D slice models (of the 3D atmosphere) with a horizontal coordinate x and vertical coordinate z. With $\bar\sigma = 1$ we get the Boussinesq scheme with Lagrangian

$$\ell(\mathbf{u},b) = \int_{\mathcal{D}}\left(\frac{1}{2}|\mathbf{u}|^2 - bz\right)\mu, \quad \mathbf{u}\in\mathfrak{X}_\mu(\mathcal{D}), \tag{2.10}$$

with buoyancy $b(x,z)$ and where $|\cdot|$ denotes the standard norm. The corresponding functional derivatives relative to the pairings (2.9) and (2.8) are $\frac{\delta\ell}{\delta\mathbf{u}} = \mathbf{u}$ and $\frac{\delta\ell}{\delta b} = -z$ leading to the equations of motion

$$\partial_t\mathbf{u} + \mathbf{u}\cdot\nabla\mathbf{u} + b\mathbf{z} = -\nabla p, \quad \mathrm{div}(\mathbf{u}) = 0, \quad \partial_t b + \mathbf{u}\cdot b = 0. \tag{2.11}$$

The full derivation of these equations can be found in [7].

Choosing $\bar{\sigma} = \bar{\rho}$ recovers the anelastic scheme with Lagrangian

$$\ell(\mathbf{u}, \theta) = \int_{\mathcal{D}} \left(\frac{1}{2}|\mathbf{u}|^2 - c_p \bar{\pi}\theta \right) \bar{\rho}\mu, \quad \mathbf{u} \in \mathfrak{X}_{\bar{\rho}\mu}(\mathcal{D}), \tag{2.12}$$

where $\bar{\pi}(z)$ is the background Exner pressure such that $c_p \frac{\partial \bar{\pi}}{\partial z} = -\frac{g}{\bar{\theta}}$ for the specific heat c_p and gravity g. Here, the thermodynamical variables are represented as variations $'$ around a vertically varying reference state, denoted with $\bar{}$, i.e. they are expanded as $\pi(x, z, t) = \bar{\pi}(z) + \pi(x, z, t)'$, $\theta(x, z, t) = \bar{\theta}(z) + \theta(x, z, t)'$, and $\rho(x, z, t) = \bar{\rho}(z) + \rho(x, z, t)'$. The functional derivatives here are $\frac{\delta \ell}{\delta \mathbf{u}} = \mathbf{u}$ and $\frac{\delta \ell}{\delta \theta} = -c_p \bar{\pi}$, leading to the equations of motion

$$\partial_t \mathbf{u} + \mathbf{u} \cdot \nabla \mathbf{u} + \nabla(c_p \bar{\theta} \pi') = g \frac{\theta'}{\bar{\theta}} \mathbf{z}, \quad \operatorname{div}(\bar{\rho}\mathbf{u}) = 0, \quad \partial_t \theta + \mathbf{u} \cdot \nabla \theta = 0. \tag{2.13}$$

This form of anelastic equations is equivalent to those in [22].

Finally, $\bar{\sigma} = \bar{\rho}\bar{\theta}$ gives the pseudo-incompressible scheme with Lagrangian

$$\ell(\mathbf{u}, \theta) = \int_{\mathcal{D}} \frac{1}{\theta} \left(\frac{1}{2}|\mathbf{u}|^2 - gz \right) \bar{\rho}\bar{\theta}\mu, \quad \mathbf{u} \in \mathfrak{X}_{\bar{\rho}\bar{\theta}\mu}(\mathcal{D}), \tag{2.14}$$

with functional derivatives $\frac{\delta \ell}{\delta \mathbf{u}} = \frac{1}{\theta}\mathbf{u}$ and $\frac{\delta \ell}{\delta \theta} = -\frac{1}{\theta^2}\left(\frac{1}{2}|\mathbf{u}|^2 - gz\right)$. This gives the equation of motion

$$\partial_t \mathbf{u} + \mathbf{u} \cdot \nabla \mathbf{u} + c_p \theta \nabla \pi' = g \frac{\theta'}{\bar{\theta}} \mathbf{z}, \quad \operatorname{div}(\bar{\rho}\bar{\theta}\mathbf{u}) = 0, \quad \partial_t \theta + \mathbf{u} \cdot \nabla \theta = 0, \tag{2.15}$$

which recover those introduced by [10].

3 Variational discretization

Analogously to above, we develop the discrete variational principle for soundproof models with the general parameter $\bar{\sigma}$.

Approximation of diffeomorphism group for soundproof flows. Given a domain $\mathcal{D}$ and a mesh $\mathbb{M}$, we approximate the weighed diffeomorphism group $G_{\bar{\sigma}\mu} = \operatorname{Diff}_{\bar{\sigma}\mu}(\mathcal{D})$ by the finite dimensional Lie group

$$\mathsf{D}_{\bar{\sigma}}(\mathbb{M}) := \left\{ q \in \mathrm{GL}(N)^+ \mid q \cdot \mathbf{1} = \mathbf{1} \text{ and } q^{\mathsf{T}} \Omega^{\bar{\sigma}} q = \Omega^{\bar{\sigma}} \right\},$$

with $\bar{\sigma} = 1$ in the Boussinesq (incompressible) case, $\bar{\sigma} = \bar{\rho}$ in the anelastic, and $\bar{\sigma} = \bar{\rho}\bar{\theta}$ in the pseudo-incompressible case, using the definitions of weighted cell-volumes:

$$\Omega_i := \int_{C_i} d\mathbf{x}, \qquad \Omega_i^{\bar{\rho}} := \int_{C_i} \bar{\rho}(z) d\mathbf{x}, \quad \text{and} \quad \Omega_i^{\bar{\rho}\bar{\theta}} := \int_{C_i} \bar{\rho}(z)\bar{\theta}(z) d\mathbf{x}. \tag{3.1}$$

The latter definitions are diagonal matrices with a reference density $\bar{\rho}(z)$, and a reference potential temperature $\bar{\theta}(z)$, while q denotes the approximation of the diffeomorphism φ as explained in the following.

The basic idea to find such approximation of the Lie group $G_{\bar{\sigma}\mu}$ is to discretize the representation on functions $\mathcal{F}(\mathcal{D})$ [26]: for $\varphi \in \mathrm{Diff}_{\bar{\sigma}\mu}(\mathcal{D})$

$$L_\varphi : \mathcal{F}(\mathcal{D}) \to \mathcal{F}(\mathcal{D}), \quad L_\varphi(f) := f \circ \varphi^{-1}.$$

This continuous linear action L_φ of volume-preserving diffeomorphisms $\mathrm{Diff}_{\bar{\sigma}\mu}(\mathcal{D})$ ($\varphi^*(\bar{\sigma}\mu) = \bar{\sigma}\mu$) on the space $\mathcal{F}(\mathcal{D})$ of functions on $\mathcal{D}$ has the following two key properties:
(1) $\langle L_\varphi(f), L_\varphi(g)\rangle_{L^2} = \langle f, g\rangle_{L^2}$ (i.e. the inner product of functions is preserved),
(2) $L_\varphi(C) = C$ (i.e. any constant function C remains constant).

We start with the discretization of $\mathcal{F}(\mathcal{D})$: for a mesh $\mathbb{D}$ with N cells, the discrete function comprises one value per cell and is given by

$$f \in \mathcal{F}(\mathcal{D}) \rightsquigarrow (F_1, ..., F_N) \in \mathbb{R}^N.$$

The discrete L^2 inner product for the discrete functions $F, G \in \mathbb{R}^N$ that approximate the continuous one $(,)$ for the continuous functions f, g is given by

$$(f, g)_{\bar{\sigma}} \rightsquigarrow \langle F, G\rangle_{\bar{\sigma}} := F^{\mathsf{T}} \Omega^{\bar{\sigma}} G = \sum_{i=1}^{N} F_i \Omega_i^{\bar{\sigma}} G_i, \quad F, G \in \mathbb{R}^N. \tag{3.2}$$

The discrete diffeomorphism group $\mathrm{D}_{\bar{\sigma}}(\mathbb{M})$, with elements $q \in \mathrm{D}_{\bar{\sigma}}(\mathbb{M})$ that are $N \times N$ matrices, is such that its action on a discrete function $F \in \mathbb{R}^N$, by matrix multiplication $q \cdot F$, is an approximation of the linear map L_φ acting on f, as illustrated by the following diagram:

$$\begin{array}{ccc} f \in \mathcal{F}(\mathcal{D}) & \xrightarrow{\mathrm{Diff}_{\bar{\sigma}}(\mathcal{D})} & L_\varphi(f) \in \mathcal{F}(\mathcal{D}) \\ \Big\downarrow \text{Discretization} & & \Big\downarrow \text{Discretization} \\ F \in \mathbb{R}^N & \xrightarrow{\mathrm{D}_{\bar{\sigma}}(\mathbb{M})} & q \cdot F \in \mathbb{R}^N \end{array}$$

and assume properties $(1)'$ and $(2)'$

$$(1)' \quad \langle q \cdot F, q \cdot G\rangle_{\bar{\sigma}} = \langle F, G\rangle_{\bar{\sigma}} \rightsquigarrow q^{\mathsf{T}} \Omega^{\bar{\sigma}} q = \Omega^{\bar{\sigma}};$$

$$(2)' \quad q \cdot \mathbf{1} = \mathbf{1} \rightsquigarrow \sum_{j=1}^{N} q_{ij} = 1,$$

with unit function $\mathbf{1} = (1_1, ..., 1_N)$ where $^{\mathsf{T}}$ denotes the transpose. In sum, the discrete diffeomorphism group reads

$$\mathrm{D}_{\bar{\sigma}}(\mathbb{M}) := \left\{ q \in \mathrm{GL}(N)^+ \;\middle|\; q^{\mathsf{T}} \Omega^{\bar{\sigma}} q = \Omega^{\bar{\sigma}}, \;\; q \cdot \mathbf{1} = \mathbf{1} \right\}$$

where $\mathrm{GL}(N)^+$ is the group of invertible $N \times N$ matrices with positive determinant. $\mathbf{1}$ denotes the constant column vector $(1, ..., 1)^{\mathsf{T}}$.

Vector field representation by Lie algebras Elements of the associated discrete Lie algebra $\mathfrak{d}_{\bar{\sigma}}(\mathbb{D})$ to the discrete Lie group $\mathrm{D}_{\bar{\sigma}}(\mathbb{M})$ provide a discretization of weighted divergence-free velocity fields. For a $q \in \mathrm{D}_{\bar{\sigma}}(\mathbb{M})$ that approximates $\varphi \in \mathrm{Diff}_{\bar{\sigma}}(\mathcal{D})$ in the above sense, we define the (semi-discrete) *Eulerian velocity* by

$$A(t) := \dot{q}(t)\, q(t)^{-1}, \tag{3.3}$$

under the condition that its representation in terms of a matrix multiplication with discrete functions F by $A \cdot F$ approximates the directional derivatives of f along $\mathbf{u}$; i.e. for $A \to \mathbf{u}$ we have the representation $A \cdot F \to -\mathbf{u} \cdot \nabla f$. The matrices A belong to the Lie algebra

$$\mathfrak{d}_{\bar{\sigma}}(\mathbb{D}) = \left\{ A \in \mathrm{gl}(N) \;\middle|\; A^{\mathsf{T}}\Omega^{\bar{\sigma}} + \Omega^{\bar{\sigma}} A = 0, \;\; A \cdot \mathbf{1} = 0 \right\}$$

in which $\mathrm{gl}(N)$ is the group of $N \times N$ matrices. The second statement represents conservation of mass, the first statement (denoted as $\Omega^{\bar{\sigma}}$ antisymmetry) preservation of volume. Such A is a discrete representation of advection by a weighted divergence-free vector field.

As shown in [26] for the incompressible case, each matrix element A_{ij} of A represents a weighted flux of $\mathbf{u} \in \mathfrak{X}_{\bar{\sigma}}(\mathcal{D})$ in the form

$$A_{ij} \simeq -\frac{1}{2\Omega_i^{\bar{\sigma}}} \int_{D_{ij}} (\bar{\sigma}\, \mathbf{u} \cdot \mathbf{n}_{ij}) \mathrm{d}S, \tag{3.4}$$

where D_{ij} is the hyperface common to cells C_i and C_j and $\mathbf{n}_{ij}$ is the normal vector field on D_{ij} pointing from C_i to C_j, cf. 3.1.

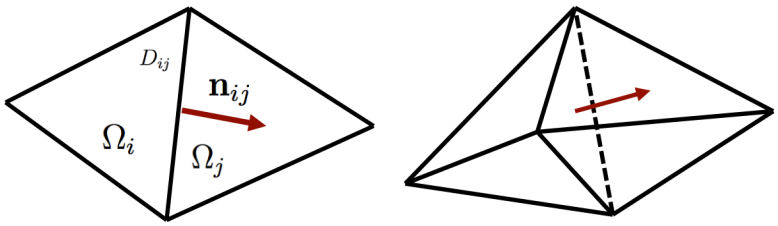

Figure 3.1: 2D and 3D sketches of the flux associated to the matrix elements A_{ij}.

In this representation, only matrix elements representing fluxes between two neighboring cells are nonzero providing us with a nonholonomic constraint $\mathcal{S} \subset \mathfrak{d}_{\bar{\sigma}}(\mathbb{M})$, i.e.

$$\mathcal{S}_{\bar{\sigma}} = \{ A \in \mathfrak{d}_{\bar{\sigma}}(\mathbb{M}) \mid A_{ij} \neq 0 \Rightarrow j \in N(i) \} \tag{3.5}$$

imposed on the Lie algebra elements and required for the variational principle, where $N(i)$ is the set of indices of those cells adjacent to cell i.

The vector field commutator $[,]$ for two adjacent cells i and j is defined by

$$[A, B]_{ij} = \sum_k (A_{ik} B_{kj} - B_{ik} A_{kj}).$$

The commutator is zero for neighboring cells since $A_{kk} = B_{kk} = 0$ due to the $\Omega^{\bar{\sigma}}$ antisymmetry. Elements of the commutator *more* than two cells away are also zero, but elements may be non-zero when cells i and j are *two* cells away from each other

Considering functions $F \in \mathbb{R}^N$ as zero form, the exterior derivative maps them to discrete 1-forms $\mathrm{d}F$ given by

$$(\mathrm{d}F)_{ij} := F_i - F_j.$$

In general, in the context of discrete diffeomorphism groups, a discrete one-form on $\mathbb{M}$ is identified with a skew-symmetric $N \times N$ matrix, cf. [7]. The space of discrete one-forms is denoted by $\Omega^1_d(\mathbb{M})$.

For the strictly positive function $\bar{\sigma} > 0$, the discrete L^2 pairing of one-forms K with vector fields A is defined via

$$\langle\langle K, A\rangle\rangle_{\bar{\sigma}} := \mathrm{Tr}\left(K^{\mathsf{T}}\Omega^{\bar{\sigma}}A\right), \quad K \in \Omega^1_d(\mathbb{M}). \tag{3.6}$$

In the cases of the Boussinesq, anelastic, and pseudo-incompressible models, the buoyancy is advected by the flow as described above by the Euler-Poincaré theory with advected quantities. To discretize this advection, we first note that the right action of $q \in \mathsf{D}_{\bar{\sigma}}(\mathbb{M})$ on a discrete function $F \in \Omega^0_d(\mathbb{M})$, denoted by $F \circ q^{-1}$, is given by the discrete pullback qF, the latter is written in terms of a matrix multiplication. Hence, the right action of q on the advected quantity $\Theta(t) \in \mathbb{R}^N$, is given by

$$\Theta(t) = q(t)\Theta_0. \tag{3.7}$$

Semidiscrete equations for soundproof models. Equations (3.3) and (3.7) allow us to write the *spatial* discrete Lagrangian as

$$\ell_d = \ell_d(A, \Theta) : \mathfrak{d}_{\bar{\sigma}}(\mathbb{M}) \times \mathbb{R}^N \to \mathbb{R}. \tag{3.8}$$

The discrete *Euler-Poincaré-d'Alembert principle* reads

$$\delta \int_0^T \ell_d(A, \Theta)dt = 0, \quad \text{for variations} \quad \delta A = \partial_t Y + [Y, A], \quad \delta\Theta = Y\Theta. \tag{3.9}$$

This Euler-Poincaré-d'Alembert principle results from a reduction of the Lagrange-d'Alembert principle under the nonholonomic constraint discussed above. As shown in [4], the variational formulation (3.9) is equivalent to the following Euler-Poincaré equations with advection:

Proposition 3.1 *A curve $(A(t), \Theta(t)) \in \mathfrak{d}_{\bar{\sigma}}(\mathbb{M}) \times \mathbb{R}^N$ is critical for the principle (3.9) if and only if there exists a discrete function $P \in \mathbb{R}^N$ such that the following equation holds*

$$\frac{d}{dt}\frac{\delta \ell_d}{\delta A_{ij}} + \left(\left[\frac{\delta \ell_d}{\delta A}\Omega^{\bar{\sigma}}, A\right](\Omega^{\bar{\sigma}})^{-1}\right)_{ij} - \frac{1}{2}\left(\frac{\delta \ell_d}{\delta \Theta_i} + \frac{\delta \ell_d}{\delta \Theta_j}\right)(\Theta_j - \Theta_i) + (P_i - P_j) = 0, \tag{3.10}$$

for all $j \in N(i)$, where the functional derivatives $\frac{\delta \ell_d}{\delta A}$ and $\frac{\delta \ell_d}{\delta \Theta}$ are computed with respect to the pairings (3.6) and (3.2).

Note that these equations are valid on any reasonable mesh (not degenerated cells). The crucial step to derive consistent schemes on such general meshes is a suitable definition of a discrete flat operator, such as introduced in [26]. We defined our schemes such to be able to apply this definition of a flat operator and hence to guarantee consistency.

4 Numerical scheme on irregular simplicial meshes

Here, we derive variational integrators in space and time for Boussinesq, anelastic, and pseudo-incompressible approximations of the Euler equations on 2D simplicial meshes. The derivations are based on the variational discretization framework introduced above for soundproof models in §3, valid for any kind of reasonable (i.e. non-degenerated) meshes.

For such triangular C-grid schemes to be derived, we use the following notations (cf. Figure 4.1):

$f_{ij} :=$ length of the triangle edge, located between triangle i and triangle j;
$h_{ij} :=$ length of the hexagonal edge connecting the circumcenters of triangle i and triangle j;
$\Omega_i :=$ area of triangle T_i.

As functional derivative of ℓ with respect to elements in $\mathfrak{d}_{\bar{\sigma}}(\mathbb{D})$ will be in the space of discrete 1-forms $\Omega^1_d(\mathbb{M})$, our derivation requires a mapping between these 1-forms and the corresponding discrete vector proxies, i.e. a flat operator $A \in \mathcal{S}_{\bar{\rho}} \mapsto A^\flat \in \Omega^1_d(\mathbb{M})$ associated to the mesh $\mathbb{M}$. As mentioned above, a consistent mapping if provided by [26]. This discrete flat operator on a 2D simplicial mesh is defined by the following two conditions

$$\begin{aligned} A^\flat_{ij} &= 2\Omega_i \frac{h_{ij}}{f_{ij}} A_{ij}, \quad \text{for } j \in N(i), \\ A^\flat_{ij} + A^\flat_{jk} + A^\flat_{ki} &= K^e_j \left\langle \omega(A^\flat), \zeta^2_e \right\rangle, \quad \text{for } i,k \in N(j),\ k \notin N(i). \end{aligned} \tag{4.1}$$

Note that this definition of matrix $A^\flat$ is skew-symmetric, hence $A^\flat \in \Omega^1_d(\mathbb{M})$. Here, we used the definitions for the constant K^e_i and the vorticity $\omega(A^\flat)$:

$$K^e_k := \frac{|\zeta_e \cap T_k|}{|\zeta_e|} \quad \text{and} \quad \left\langle \omega(A^\flat), \zeta_e \right\rangle := \sum_{h_{mn} \in \partial\zeta_e} A^\flat_{mn}, \tag{4.2}$$

in which e denotes the node common to triangles T_i, T_j, T_k and where $|\zeta_e \cap T_k|$ is the area of the intersection of T_k and the dual cell ζ_e of e (cf. Fig. 4.1 in which e is denoted by $\pm$). To calculate the vorticity, the sum is taken over the dual edges in the boundary $\partial\zeta_e$ counterclockwise around node e.

For the anelastic and pseudo-incompressible models, the first line of the definition of the flat operator (4.1) has to be slightly modified to obtain a skew-symmetric matrix; hence we write

$$A^\flat := M^{(A)}, \quad \text{for the matrix } M \text{ defined by } \quad M_{ij} := 2\Omega_i \frac{h_{ij}}{f_{ij}} A_{ij}, \tag{4.3}$$

in which $(\cdot)^{(A)}$ denotes the skew-symmetric part. This definition satisfies the properties of a flat in [26].

4.1 Boussinesq flow

From (3.10) we derive the variational discretization of the Boussinesq fluid model on irregular 2D simplicial grids. Subject to the condition of divergence free flow $\mathrm{div}_\mu(\mathbf{u}) = 0$, the Boussinesq

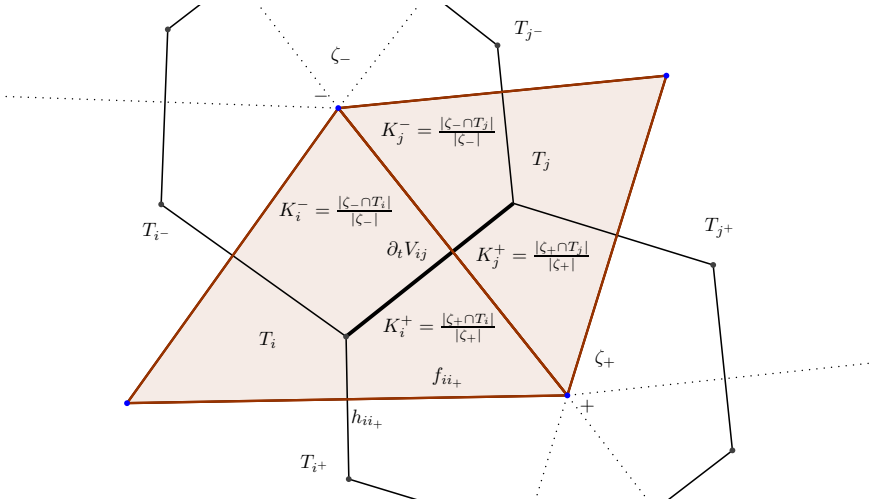

Figure 4.1: Notation and indexing conventions for the 2D simplicial mesh.

Lagrangian is given by Eqn. (2.10). The corresponding discrete Lagrangian is hence given by $\ell_d : \mathfrak{d}(\mathbb{M}) \times \mathbb{R}^N \to \mathbb{R}$,

$$\ell_d(A, B) = \frac{1}{2} \left\langle\!\left\langle A^\flat, A \right\rangle\!\right\rangle_1 - \langle B, Z \rangle_1 , \tag{4.4}$$

using the duality parings (3.6) and (3.2) for $\bar{\sigma} = 1$ and in which $B \in \mathbb{R}^N$ is the discrete buoyancy function and Z is the discrete height function such that Z_i denotes the z-coordinate of the center of cell C_i. The first term in (4.4) is the discrete kinetic energy terms, which requires the use of the flat operator (4.1), the second term is associated to the buoyancy force.

The discrete functional derivatives of the discrete Boussinesq Lagrangian (4.4) read

$$\frac{\delta \ell_d}{\delta A_{ij}} = A^\flat_{ij} \quad \text{and} \quad \frac{\delta \ell_d}{\delta B_i} = -Z_i.$$

Substituting them in the Euler-Poincaré equation (3.10) while using the discrete flat operator (4.1) yields the discrete equations of motion, written in covariant form [4]

$$\begin{cases} \partial_t A^\flat_{ij} + \left\langle \omega(A^\flat), \zeta^2_- \right\rangle \left(K^-_i A_{ii_-} + K^-_j A_{jj_-} \right) - \left\langle \omega(A^\flat), \zeta^2_+ \right\rangle \left(K^+_i A_{ii_+} + K^+_j A_{jj_+} \right) \\ \qquad\qquad = -\dfrac{Z_i + Z_j}{2}(B_j - B_i) + (\tilde{P}_j - \tilde{P}_i), \quad \text{for all } j \in N(i), \\ \partial_t B_i - \displaystyle\sum_{j \in N(i)} A_{ij} B_j = 0. \end{cases} \tag{4.5}$$

$\tilde{P}$ is related to P in (3.10) by $\tilde{P}_i = P_i + \sum_{k \in N(i)} A^\flat_{ik} A_{ik}$, this latter relation is however not required for solving the set of equations (see disussion below).

Further we notice that both the elements of A and $A^\flat$ can be represented in form of a velocity degree of freedom normal to the triangle edges and denoted by V_{ij} with positive orientation when pointing from cell i to j. In detail, given the relation between the Lie algebra element $A \in \mathfrak{d}(\mathbb{M})$ and the velocity $\mathbf{u}$ by $A_{ij} \simeq -\frac{1}{2\Omega_i} \int_{f_{ij}} (\mathbf{u} \cdot \mathbf{n}) \mathrm{d}S$, these relations are given by

$$A_{ij} = -\frac{1}{2\Omega_i} f_{ij} V_{ij} \quad \text{and} \quad A^\flat_{ij} = -h_{ij} V_{ij} \quad \text{for} \quad i \in N(j). \tag{4.6}$$

Note that $\Omega_i A_{ij} = -\Omega_j A_{ji}$, for all i, j, translate to $V_{ij} = -V_{ji}$ and $\sum_{j\in N(i)} A_{ij} = 0$ to $\sum_{j\in N(i)} f_{ij} V_{ij} = 0$, which corresponds to the divergence free condition. Using the relations (4.6), gives the semidiscrete Boussinesq equations, written in vector-matrix form, as

$$\partial_t V_{ij} + \mathrm{Adv}_{\mathrm{b}}(V)_{ij} = \mathrm{F}_{\mathrm{b}}(B)_{ij} - (\nabla_{\mathrm{b}}\tilde{P})_{ij}, \tag{4.7}$$

where we defined

$$\begin{aligned}
\mathrm{Adv}_{\mathrm{b}}(V)_{ij} &:= -\frac{1}{h_{ij}|\zeta^2_-|}\Big(\sum_{\zeta^1_{mn}\in\partial\zeta^2_-} h_{mn}V_{mn}\Big)\left(\frac{|\zeta^2_-\cap T_i|}{2\Omega_i} f_{ii_-}V_{ii_-} + \frac{|\zeta^2_-\cap T_j|}{2\Omega_j} f_{jj_-}V_{jj_-}\right)\\
&\quad + \frac{1}{h_{ij}|\zeta^2_+|}\Big(\sum_{\zeta^1_{mn}\in\partial\zeta^2_+} h_{mn}V_{mn}\Big)\left(\frac{|\zeta^2_+\cap T_i|}{2\Omega_i} f_{ii_+}V_{ii_+} + \frac{|\zeta^2_+\cap T_j|}{2\Omega_j} f_{jj_+}V_{jj_+}\right),\\
\mathrm{F}_{\mathrm{b}}(B)_{ij} &:= \frac{Z_i + Z_j}{2h_{ij}}(B_j - B_i),\\
(\nabla_{\mathrm{b}}\tilde{P})_{ij} &:= \frac{1}{h_{ij}}(\tilde{P}_j - \tilde{P}_i).
\end{aligned}$$

As the time discretization of the advection equation for B will be based on the Cayley map (4.16), we skip its explicit vector-matrix representation here.

We used everywhere the index b, referring to Boussinesq, to distinguish from the expressions occurring further below for the other two models.

4.2 Anelastic flow

The anelastic Lagrangian is given in (2.12). We approximate it by the discrete Lagrangian $\ell_d : \mathfrak{d}_{\bar\rho}(\mathbb{M}) \times \mathbb{R}^N \to \mathbb{R}$:

$$\ell_d(A,\Theta) = \frac{1}{2}\left\langle\!\left\langle A^\flat, A\right\rangle\!\right\rangle_{\bar\rho} - c_p\left\langle \bar\Pi, \Theta\right\rangle_{\bar\rho} = \frac{1}{2}\sum_{ij} A^\flat_{ij}A_{ij}\Omega^{\bar\rho}_i - c_p\sum_i \bar\Pi_i\Theta_i\Omega^{\bar\rho}_i, \tag{4.8}$$

with duality parings (3.6) and (3.2) for $\bar\sigma = \bar\rho$ and where $\bar\Pi \in \mathbb{R}^N$ is a discretization of the reference value $\bar\pi(z)$ of the Exner pressure. The functional derivatives of ℓ_d with respect to $\langle\!\langle\,,\rangle\!\rangle_{\bar\rho}$ and $\langle\,,\rangle_{\bar\rho}$, respectively, read

$$\frac{\delta\ell_d}{\delta A_{ij}} = A^\flat_{ij} \quad \text{and} \quad \frac{\delta\ell}{\delta\Theta_i} = -c_p\bar\Pi_i.$$

Substituting them in (3.10) while using the modified flat operator (4.3) leads to the semi-discrete equations for the anelastic equations [4]

$$\begin{cases}
\partial_t A^\flat_{ij} + \left\langle\omega(A^\flat), \zeta^2_-\right\rangle\left(K^-_i A_{ii_-} + K^-_j A_{jj_-}\right) - \left\langle\omega(A^\flat), \zeta^2_+\right\rangle\left(K^+_i A_{ii_+} + K^+_j A_{jj_+}\right)\\
\qquad\qquad = -c_p\dfrac{\bar\Pi_i + \bar\Pi_j}{2}(\Theta_j - \Theta_i) + (\tilde{P}_j - \tilde{P}_i), \quad \text{for all } j\in N(i),\\
\partial_t\Theta_i - \displaystyle\sum_{j\in N(i)} A_{ij}\Theta_j = 0,
\end{cases} \tag{4.9}$$

in which $\Omega^{\bar\rho}_i A_{ij} = -\Omega^{\bar\rho}_j A_{ji}$, for all i, j, and where $\sum_{j\in N(i)} A_{ij} = 0\ \forall i$, is the discrete version of $\mathrm{div}_\mu(\bar\rho\mathbf{u}) = 0$. $\tilde{P}$ is related to P in (3.10) as in the Boussinesq case.

For the equations' representation in vector-matrix form, we note that the Lie algebra element $A \in \mathfrak{d}_{\bar\rho}(\mathbb{M})$ and the velocity $\mathbf{u}$ are related as $A_{ij} \simeq -\frac{1}{2\Omega_i^{\bar\rho}} \int_{f_{ij}} (\bar\rho\, \mathbf{u}\cdot\mathbf{n}) \mathrm{d}S$ such that A and $A^\flat$ are related to V_{ij} as

$$A_{ij} = -\frac{1}{2\Omega_i^{\bar\rho}} f_{ij}\bar\rho_{ij} V_{ij} \quad \text{and} \quad A^\flat_{ij} = -h_{ij}\sigma^{\mathrm{a}}_{ij} V_{ij} \tag{4.10}$$

with definitions $\bar\rho_{ij} := \frac{\bar\rho_i + \bar\rho_j}{2}$ for $\bar\rho_i := \Omega_i^{\bar\rho}/\Omega_i$, the latter denotes the mean value of $\bar\rho(z)$ over cell C_i, and $\sigma^{\mathrm{a}}_{ij} := \frac{\bar\rho_{ij}}{2}\left(\frac{1}{\bar\rho_i} + \frac{1}{\bar\rho_j}\right)$. Hence, the momentum equation in (4.9) reads

$$\partial_t V_{ij} + \mathrm{Adv}_{\mathrm{a}}(V)_{ij} = \mathrm{F}_{\mathrm{b}}(\Theta)_{ij} - (\nabla_{\mathrm{a}}\tilde P)_{ij}, \tag{4.11}$$

where we defined

$$\begin{aligned}
&\mathrm{Adv}_{\mathrm{a}}(V)_{ij} := \\
&-\frac{1}{\sigma^{\mathrm{a}}_{ij} h_{ij} |\zeta^2_-|}\Big(\sum_{\zeta^1_{mn}\in\partial\zeta^2_-} \sigma^{\mathrm{a}}_{mn} h_{mn} V_{mn}\Big)\left(\frac{|\zeta^2_-\cap T_i|}{2\Omega_i\bar\rho_i} f_{ii_-}\bar\rho_{ii_-} V_{ii_-} + \frac{|\zeta^2_-\cap T_j|}{2\Omega_j\bar\rho_j} f_{jj_-}\bar\rho_{jj_-} V_{jj_-}\right) \\
&+\frac{1}{\sigma^{\mathrm{a}}_{ij} h_{ij} |\zeta^2_+|}\Big(\sum_{\zeta^1_{mn}\in\partial\zeta^2_+} \sigma^{\mathrm{a}}_{mn} h_{mn} V_{mn}\Big)\left(\frac{|\zeta^2_+\cap T_i|}{2\Omega_i\bar\rho_i} f_{ii_+}\bar\rho_{ii_+} V_{ii_+} + \frac{|\zeta^2_+\cap T_j|}{2\Omega_j\bar\rho_j} f_{jj_+}\bar\rho_{jj_+} V_{jj_+}\right), \\
&\mathrm{F}_{\mathrm{a}}(\Theta)_{ij} := \frac{c_p}{\sigma^{\mathrm{a}}_{ij} h_{ij}} \frac{\bar\Pi_i + \bar\Pi_j}{2}(\Theta_j - \Theta_i), \\
&(\nabla_{\mathrm{a}}\tilde P)_{ij} := \frac{1}{\sigma^{\mathrm{a}}_{ij} h_{ij}}(\tilde P_j - \tilde P_i).
\end{aligned}$$

Also here, we skip an explicit representation of the advection equation for θ as it will be time discretization by the Cayley map (4.16) too.

4.3 Pseudo-incompressible flow

Finally, the Lagrangian for the pseudo-incompressible model (2.14) will be approximated by the discrete Lagrangian $\ell_d : \mathfrak{d}_{\bar\rho}(\mathbb{M}) \times \mathbb{R}^N \to \mathbb{R}$:

$$\ell_d(A,\Theta) = \frac{1}{2}\sum_{ij}\frac{1}{\Theta_i} A^\flat_{ij} A_{ij} \Omega_i^{\bar\rho\bar\theta} - g\sum_i \frac{1}{\Theta_i} Z_i \Omega_i^{\bar\rho\bar\theta}, \tag{4.12}$$

in which $Z \in \mathbb{R}^N$ is a discretization of the height z and in which we have explicity written the dual parings by using the volumes $\Omega_i^{\bar\rho\bar\theta}$. For $\bar\sigma = \bar\rho\bar\theta$, the functional derivatives of ℓ_d with respect to the pairings $\langle\!\langle\, , \rangle\!\rangle_{\bar\rho\bar\theta}$ and $\langle\, , \rangle_{\bar\rho\bar\theta}$ give, respectively

$$\frac{\delta \ell_d}{\delta A_{ij}} = \frac{1}{2}\left(\frac{1}{\Theta_i} + \frac{1}{\Theta_j}\right) A^\flat_{ij} =: M_{ij} \quad \text{and} \quad \frac{\delta \ell}{\delta \Theta_i} = \frac{1}{\Theta_i^2}\Big(gZ_i - k_i\Big), \quad k_i := \frac{1}{2}\sum_j A^\flat_{ij} A_{ij}.$$

The substitution of these functional derivatives in (3.10) while using the modifed flat operator (4.3) leads to the semi-discrete equations of the pseudo-incompressible system [4]

$$\begin{cases} \partial_t M_{ij} + \langle \omega(M), \zeta_-^2 \rangle \left(K_i^- A_{ii_-} + K_j^- A_{jj_-} \right) - \langle \omega(M), \zeta_+^2 \rangle \left(K_i^+ A_{ii_+} + K_j^+ A_{jj_+} \right) \\ \qquad\qquad = \frac{1}{2} \left(\frac{gZ_i - k_i}{\Theta_i^2} + \frac{gZ_j - k_j}{\Theta_j^2} \right) (\Theta_j - \Theta_i) + (\tilde{P}_j - \tilde{P}_i), \quad \text{for all } j \in N(i)\,, \\ M_{ij} = \frac{1}{2} \left(\frac{1}{\Theta_i} + \frac{1}{\Theta_j} \right) A_{ij}^\flat, \\ \partial_t \Theta_i - \sum_{j \in N(i)} A_{ij} \Theta_j = 0, \end{cases} \tag{4.13}$$

where $\Omega_i^{\bar\rho\bar\theta} A_{ij} = -\Omega_j^{\bar\rho\bar\theta} A_{ji}$, for all i, j, and where $\mathrm{div}_\mu(\bar\rho\bar\theta\mathbf{u}) = 0$ is approximated by $\sum_{\in N(i)} A_{ij} = 0$, for all i. $\tilde{P}$ is related to P in (3.10) by $\tilde{P}_i = P_i + \sum_{k \in N(i)} M_{ik} A_{ik}$.

To write also this covariant momentum equation in vector-matrix form, we recall that the Lie algebra element $A \in \mathfrak{d}_{\bar\rho\bar\theta}(\mathbb{M})$ and the velocity $\mathbf{u}$ are related here as $A_{ij} \simeq -\frac{1}{2\Omega_i^{\bar\rho\bar\theta}} \int_{f_{ij}} (\bar\rho\bar\theta\, \mathbf{u} \cdot \mathbf{n}) \mathrm{d}S$. The relation to the velocity V_{ij} is hence

$$A_{ij} = -\frac{1}{2\Omega_i^{\bar\rho\bar\theta}} f_{ij} \overline{\rho\theta}_{ij} V_{ij} \quad \text{and} \quad A_{ij}^\flat = -h_{ij} \sigma_{ij}^{\mathrm{pi}} V_{ij} \tag{4.14}$$

with $\overline{\rho\theta}_{ij} := \frac{\overline{\rho\theta}_i + \overline{\rho\theta}_j}{2}$ for $\overline{\rho\theta}_i := \Omega_i^{\bar\rho\bar\theta}/\Omega_i$, the mean value of $\bar\rho(z)\bar\theta(z)$ over cell C_i. Moreover, we have $\sigma_{ij}^{\mathrm{pi}} := \frac{\overline{\rho\theta}_{ij}}{2} \left(\frac{1}{\overline{\rho\theta}_i} + \frac{1}{\overline{\rho\theta}_j} \right)$. Then, the semidiscrete pseudo-incompressible momentum equation (4.13) becomes

$$\partial_t (\widetilde{\Theta}_{ij} V_{ij}) + \mathrm{Adv}_{\mathrm{pi}}(V, \Theta)_{ij} = \mathrm{F}_{\mathrm{pi}}(\Theta)_{ij} - (\nabla_{\mathrm{pi}} \tilde{P})_{ij}, \tag{4.15}$$

where we defined

$$\begin{aligned} &\mathrm{Adv}_{\mathrm{pi}}(V, \Theta)_{ij} := \\ &-\frac{1}{\sigma_{ij}^{\mathrm{pi}} h_{ij} |\zeta_-^2|} \Big(\sum_{\zeta_{mn}^1 \in \partial \zeta_-^2} \sigma_{mn}^{\mathrm{pi}} h_{mn} \widetilde{\Theta}_{mn} V_{mn} \Big) \left(\frac{|\zeta_-^2 \cap T_i|}{2\Omega_i \overline{\rho\theta}_i} f_{ii_-} \overline{\rho\theta}_{ii_-} V_{ii_-} + \frac{|\zeta_-^2 \cap T_j|}{2\Omega_j \overline{\rho\theta}_j} f_{jj_-} \overline{\rho\theta}_{jj_-} V_{jj_-} \right) \\ &+\frac{1}{\sigma_{ij}^{\mathrm{pi}} h_{ij} |\zeta_+^2|} \Big(\sum_{\zeta_{mn}^1 \in \partial \zeta_+^2} \sigma_{mn}^{\mathrm{pi}} h_{mn} \widetilde{\Theta}_{mn} V_{mn} \Big) \left(\frac{|\zeta_+^2 \cap T_i|}{2\Omega_i \overline{\rho\theta}_i} f_{ii_+} \overline{\rho\theta}_{ii_+} V_{ii_+} + \frac{|\zeta_+^2 \cap T_j|}{2\Omega_j \overline{\rho\theta}_j} f_{jj_+} \overline{\rho\theta}_{jj_+} V_{jj_+} \right), \\ &\mathrm{F}_{\mathrm{pi}}(V, \Theta)_{ij} := -\frac{1}{2\sigma^{\mathrm{pi}} h_{ij}} \left(\frac{gZ_i - k_i}{\Theta_i^2} + \frac{gZ_j - k_j}{\Theta_j^2} \right) (\Theta_j - \Theta_i), \\ &(\nabla_{\mathrm{a}} \tilde{P})_{ij} := \frac{1}{\sigma_{ij}^{\mathrm{pi}} h_{ij}} (\tilde{P}_j - \tilde{P}_i). \end{aligned}$$

Also here, the time discretization of the advection equation for θ is treated by using the Cayley map (4.16) and explicitly shown here.

4.4 Time integration and Poisson solvers

Since the spatial discretization has been realized in a structure-preserving way, a corresponding temporal variational discretization follows by applying the general discrete (in time) Euler-

Poincaré approach, as it has be done in [12], [7] to which we refer for a detailed treatment. Hence, the temporal scheme consists of the following two steps.

Given the time t and a time step size Δt, we first compute $\Theta^{t+1} = \tau(\Delta t A^t)\Theta^t$ (with $\Theta = B$ in case of Boussinesq), in which τ is the Cayley transform. To this end we represent τ by the equation:

$$(I - \frac{1}{2}\Delta t A^t)\Theta^{t+1} = (I + \frac{1}{2}\Delta t A^t)\Theta^t. \tag{4.16}$$

with I the identity matrix (cf. [7] for more details). In the second step, the following update equations are solved. They are given in explicit form for the Boussinesq/anelastic schemes by

$$\frac{V_{ij}^{t+1} - V_{ij}^t}{\Delta t} = -\frac{1}{2}\,\mathrm{Adv}_{\mathrm{b/a}}(V^{t+1})_{ij} - \frac{1}{2}\,\mathrm{Adv}_{\mathrm{b/a}}(V^t)_{ij} - \mathrm{F}_{\mathrm{b/a}}(\Theta^{t+1})_{ij} - (\nabla_{\mathrm{b/a}}\tilde{P}^{t+1})_{ij}\ , \tag{4.17}$$

and for the pseudo-incompressible equation by

$$\begin{aligned}\frac{\widetilde{\Theta}_{ij}^{t+1}V_{ij}^{t+1} - \widetilde{\Theta}_{ij}^{t}V_{ij}^{t}}{\Delta t} = -\frac{1}{2}\,\mathrm{Adv}_{\mathrm{pi}}(V^{t+1},\Theta^{t+1}) - \frac{1}{2}\,\mathrm{Adv}_{\mathrm{pi}}(V^t,&\Theta^t)_{ij} \\ &- \mathrm{F}_{\mathrm{pi}}(V^t,\Theta^{t+1})_{ij} - (\nabla_{\mathrm{pi}}\tilde{P}^{t+1})_{ij}\ .\end{aligned} \tag{4.18}$$

This time update scheme, derived from discrete Euler-Poincaré equations, is analogous to a Crank-Nicolson time update scheme. To solve these implicit equations, we proceed as follows. Noting that Θ^{t+1} has been calculated first and is thus known, we rearrange the equations into known and unknown parts as

$$\begin{aligned}V_{ij}^{t+1} = \underbrace{V_{ij}^t - \frac{\Delta t}{2}\,\mathrm{Adv}_{\mathrm{b/a}}(V^t)_{ij} - \Delta t\,\mathrm{F}_{\mathrm{b/a}}(\Theta^{t+1})_{ij}}_{=:\mathrm{G}_{\mathrm{b/a}}(V^t)_{ij}} &- \frac{\Delta t}{2}\,\mathrm{Adv}_{\mathrm{b/a}}(V^{t+1})_{ij} \\ &- \Delta t(\nabla_{\mathrm{b/a}}P^{t+1})_{ij}\,,\end{aligned} \tag{4.19}$$

and similarly for the pseudo-incompressible equations:

$$\begin{aligned}V_{ij}^{t+1} = \underbrace{\frac{\widetilde{\Theta}^t}{\widetilde{\Theta}^{t+1}}V_{ij}^t - \frac{\Delta t}{2\widetilde{\Theta}^{t+1}}\,\mathrm{Adv}_{\mathrm{pi}}(V^t,\Theta^t)_{ij} - \frac{\Delta t}{\widetilde{\Theta}^{t+1}}\,\mathrm{F}_{\mathrm{pi}}(V^t,\Theta^{t+1})_{ij}}_{=:\mathrm{G}_{\mathrm{pi}}(V^t)_{ij}} \\ - \frac{\Delta t}{2\widetilde{\Theta}^{t+1}}\,\mathrm{Adv}_{\mathrm{pi}}(V^{t+1},\Theta^{t+1})_{ij} - \frac{\Delta t}{\widetilde{\Theta}^{t+1}}(\nabla_{\mathrm{pi}}P^{t+1})_{ij}\ .\end{aligned} \tag{4.20}$$

We can summaries the edge values into vector arrays, which we will indicate by omitting the notation ij. Then, we solve these vector equations for Boussinesq, anelasic, and pseudo-incompressible schemes by a *fixed point iteration*, given by the following algorithm:

1. Start loop over $k = 0$ with initial guess at t: $V_{k=0}^* = V^t$ and $P_{k=0}^* = 0$

2. Calculate tentative velocity $\widetilde{V}_k^*$:

   - Boussinesq/anelastic: $\widetilde{V}_k^* = \mathrm{G}_{\mathrm{b/a}}(V^t) - \frac{\Delta t}{2}\,\mathrm{Adv}_{\mathrm{b/a}}(V_k^*)$;

- Pseudo-incompressible: $\widetilde{V}_k^* = \mathrm{G}_{\mathrm{pi}}(V^t) - \frac{\Delta t}{2\widetilde{\Theta}^{t+1}} \mathrm{Adv}_{\mathrm{pi}}(V_k^*, \Theta^{t+1})$;

3. Calculate pressure P_{k+1}^* by solving the Poisson equation:

   - Boussinesq ($\widehat{\rho} = 1$)/anelastic ($\widehat{\rho} = \bar{\rho}$): $\nabla \cdot \left(\widehat{\rho} \nabla_{\mathrm{b/a}} P_{k+1}^*\right) = \frac{1}{\Delta t} \nabla \cdot (\widehat{\rho} \widetilde{V}_k^*)$;
   - Pseudo-incompressible: $\nabla \cdot \left(\frac{\bar{\rho}\bar{\Theta}}{\widetilde{\Theta}^{t+1}} \nabla_{\mathrm{pi}} P_{k+1}^*\right) = \frac{1}{\Delta t} \nabla \cdot (\bar{\rho}\bar{\Theta} \widetilde{V}_k^*)$;

4. Update velocity and set $k + 1 = k$:

   - Boussinesq/anelastic: $V_{k+1}^* = \widetilde{V}_k^* - \Delta t \nabla_{\mathrm{b/a}} P_{k+1}^*$;
   - Pseudo-incompressible: $V_{k+1}^* = \widetilde{V}_k^* - \frac{\Delta t}{\widetilde{\Theta}^{t+1}} \nabla_{\mathrm{pi}} P_{k+1}^*$;

5. Stop loop over k if $||V_{k+1}^* - V_k^*|| < \epsilon$ for a small positive ϵ.

Substituting the tentative velocity $\widetilde{V}_k^*$ into the velocity update equation (step 4), we realize that in case of convergence, i.e. $V_{k+1}^* \to V^{t+1}$ and $P_{k+1}^* \to P^{t+1}$, this algorithm indeed solves equations (4.19) and (4.20).

Please note that the Poisson equations result from multiplying the anelastic momentum equations by $\bar{\rho}$ and the pseudo-incompressible by $\bar{\rho}\bar{\Theta}$ while imposing $\nabla \cdot (\bar{\rho} V^{t+1}) = 0$ or $\nabla \cdot \left(\bar{\rho}\bar{\Theta} V^{t+1}\right) = 0$, respectively. In the latter case we additionally assumed $\widetilde{\Theta}^* = \widetilde{\Theta}^{k+1}$. The respective divergence operators, denoted as $\nabla \cdot (\widehat{\rho} V) = \sum_{j \in N(i)} \frac{\widehat{\rho}_{ij} f_{ij} V_{ij}}{\Omega_i} = 0$, with $\widehat{\rho}_{ij} = 1$, $\widehat{\rho}_{ij} = \bar{\rho}_{ij}$, and $\widehat{\rho}_{ij} = (\bar{\rho}\bar{\Theta})_{ij}$, for the Boussinesq, anelastic, and pseudo-incompressible schemes, respectively, follow directly from the corresponding definitions of A and the divergence-freeness constraint $\sum_{j \in N(i)} A_{ij} = 0$, for all i.

Being derived both spatially and temporally via the Euler-Poincaré approach, the schemes (4.17) and (4.18) admit discrete version of the Kelvin circulation theorem. We refer to [12] and [7] for detailed discussions of the discrete Kelvin circulation theorems and its application to several examples. Since the application to the present models is similar we shall not repeat it here.

5 Numerical tests

We study numerically the behavior of the variational discretization schemes for the Boussinesq, anelastic, and pseudo-incompressible equations for regular and irregular computational meshes. On various test cases we investigate the models' dynamical behavior and their conservation of mass and energy. Descending from variational principles, these schemes are supposed to conserve the latter quantities to a high degree. Moreover as these models support internal gravity waves, we are interested in a quantitative evaluation of their discrete dispersion relations.

For all ensuing test cases we perform the simulations on regular and irregular triangular meshes. The regular meshes consist of equilateral triangles of constant edge length $f = |f_{ij}|$, where $f_{ij}, j = 1, 2, 3$, denote the edges of triangle T_i (cf. notation of Section 4). The distance between neighboring vertices in x-direction is given by $f_x := f$ while the height of the triangles in z-direction is given by $f_z := \frac{\sqrt{3}}{2} f$. Given a domain size of $L_x \times L_z$, in which L_x and L_z denote the domain's length in x- and z-directions, respectively, the *mesh resolution*, denoted by $2 \cdot N_x \times N_z$ for $N_x := L_x / f_x$ and $N_y := L_z / f_z$, corresponds to the number of triangular cells.

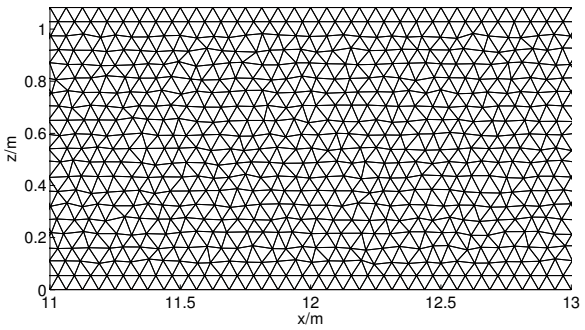

Figure 5.1: Section of central part of irregular mesh (ii) with $\max_{\mathbf{x}\in\Omega} \Delta h(\mathbf{x}) \leq 7$ for a resolution of $2 \cdot 384 \times 20$ triangular cells.

To construct irregular meshes, we start from a regular one and randomly move the regularly distributed *internal* vertices – i.e. vertices that do *not* belong to boundary cells – from point $\mathbf{x_i} = (x_i, z_i)$ to $\mathbf{x_i} + \delta\mathbf{x_i}$ within the bounds $|\delta x_i| < c \cdot f_x \cdot r$ and $|\delta z_i| < c \cdot f_z \cdot r$, for a positive constant c and some random number $r \in [-0.5, 0.5]$. Leaving the boundary triangles regular is not necessary in terms of the discretization schemes, however it eases the way of how we implemented the boundary conditions (a more general treatment is possible, but we leave it to future work).

For our studies we use (i) $c = 0.1$ and (ii) $c = 0.2$ to construct meshes with different degrees of irregularity. The resulting distortion of the meshes can be quantified using a grid quality measure introduced in [2] that measures the distortion of the dual cells: $\Delta h(\mathbf{x}) := \frac{\max_j \ h_{ij}}{\min_j \ h_{ij}}$, in which h_{ij} is the length of dual edge j of dual cell ζ_i^2 that contains point $\mathbf{x}$. High values of Δh indicate strongly deformed cells. As such cells may impact on the quality of the simulations, as shown in [2], we apply for the advection dominated test cases in Section 5.3 the irregular mesh (i), where we restrict the irregularity of the grid to $\max_{\mathbf{x}\in\Omega} \Delta h(\mathbf{x}) \leq 1.5$ by setting $c = 0.1$. In contrast to such rather smooth grid, we apply for the hydrostatic adjustment test cases in Section 5.1 the irregular mesh (ii) for $c = 0.2$ with $\max_{\mathbf{x}\in\Omega} \Delta h(\mathbf{x}) \leq 7$ (cf. Figure 5.1) in order to illustrate that our variational schemes are also stable on strongly deformed meshes while conserving mass and total energy to a high degree.

5.1 Internal gravity waves by hydrostatic adjustment

An essential ingredient of the derivation of Boussinesq, anelastic and pseudo-incompressible models is the assumption of a vertically varying reference state that is in hydrostatic balance, i.e. the gravitational and pressure terms compensate each other. When out of equilibrium, the system tends to a balanced state by the so-called hydrostatic adjustment process [18] by emitting internal gravity waves.

Here, we investigate the above derived variational integrators using the hydrostatic adjustment process. We study their dynamical behavior, long term energy and mass conservation properties, and their discrete dispersion relations. To this end, we initialize the Boussinesq scheme as in [7], and adapt the therein suggested test case to suit also for the anelastic and pseudo-incompressible schemes. This will allow us to compare quantitatively the simulation results of our schemes with each other and with those of [7].

We use for the simulations in this section a computation domain of dimension $(x, z) \in \mathcal{D} = [0, L_x] \times [0, L_z], L_x = 24\,\mathrm{m}, L_z = 1\,\mathrm{m}$, while imposing periodic boundary conditions in

x-direction and free-slip boundary conditions at the upper and lower boundaries of the domain. We integrate for a time interval of 100 s (in correspondence to [7]) with a time step size of $\Delta t = 0.25$ s. Both regular and irregular computational meshes have a resolution of $2 \cdot 384 \times 20$ triangular cells (cf. Figure 5.1).

5.1.1 Hydrostatic adjustment of the Boussinesq model

Consider the Boussinesq system in hydrostatic equilibrium between a stable reference buoyancy $\bar{b}(z)$ and the pressure P_b:

$$\frac{\partial P_b}{\partial z} = -\bar{b}. \tag{5.1}$$

When out of equilibrium, the system tends to a hydrostatic balance by emitting internal gravity waves that obey the dispersion relation

$$\omega^2 = \frac{k_x^2 N_b^2}{\mathbf{k^2}} \tag{5.2}$$

with wave vector $\mathbf{k} = (k_x, k_y) \in \mathbb{Z}$ in which $N_b^2 := -\frac{d\bar{b}}{dz} = \frac{g}{\theta_0}\frac{d\bar{\theta}}{dz}$, assumed to be a constant, denotes the Brunt-Väsälä frequency for the case of Boussinesq equations. One observes that the frequencies of the internal gravity waves are bounded from above by N_b.

We further note that mass conservation is given by

$$\frac{d}{dt}\int_{\mathcal{D}} b(x,z,t)d\mathbf{x} = 0. \tag{5.3}$$

Being implicitly related to the density, we refer to this quantity, and the upcoming similar ones for anelastic and pseudo-incompressible equations, generally as mass $M(t)$. Hence, we study whether the discrete integral of b over the domain $\mathcal{D}$, denoted as mass $M(t)$, remains constant in time and whether the discrete total energy that corresponds to the energy density $E = \frac{1}{2}|\mathbf{u}|^2 + bz$ is conserved.

Initialization. Analogously to [7], we initialize the system on the basis of a hydrostatic equilibrium, given by $u_{\text{eq}}(x,z) = w_{\text{eq}}(x,z) = 0$ and $b_{\text{eq}}(x,z) = -N_b^2 z =: \bar{b}(z)$ in units $[b] = m/s^2$, on which at $t = 0$ a localized positive buoyancy disturbance $\tilde{b}(x,z)$ with compact support is superimposed. Hence, the initial buoyancy field $b(x,z,0) = \bar{b}(z) + \tilde{b}(x,z)$ with Brunt-Väsälä frequency $N_b = 1/\text{s}$ is given by the function

$$b(x,z,0) = N_b^2 \begin{cases} -z + \beta_b e^{\left(\frac{-r_0^2}{r_0^2 - r^2}\right)} & \text{if } r < r_0, \quad r^2 = (x - \frac{L_x}{2})^2 + (z - \frac{L_z}{2})^2, \\ -z & \text{if } r \geq r_0, \end{cases} \tag{5.4}$$

with parameters: $r_0 = 0.2 \cdot L_z$, $\beta_b = 0.3 \cdot L_z$, $r^2 = (x - \frac{L_x}{2})^2 + (z - \frac{L_z}{2})^2$. Note that $[z] = \text{m}$, hence the choice of $N_b = 1/\text{s}$ suggests further to set $g = 1\,\text{m/s}^2$ and $\theta_0 = 1\,\text{K}$. Given these analytical functions, the discrete function $B = \{B_i | \text{ for all triangles } T_i\}$ is obtained by setting $B_i(0) = b(x_i, z_i, 0)$ for all triangles T_i with cell centers at position (x_i, z_i).

Results. To study numerically the dispersion relation of our discrete model, we determine the Fourier transforms of a time series of the buoyancy field $b(x,z,t)$ for the time interval $t \in [0, 100\,\text{s}]$ at various locations of the computation domain $\mathcal{D}$ (similar to those chosen by [7]).

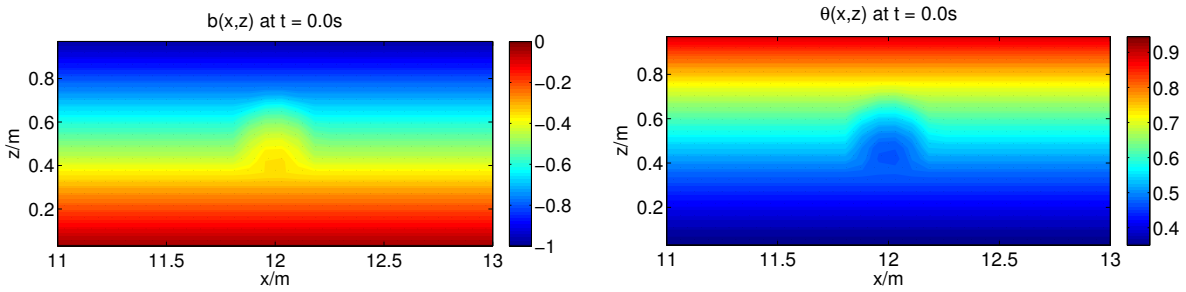

Figure 5.2: Initialization of the Boussinesq scheme by the buoyancy field $b(x, z, 0)$ shown left. Initalization of the anelasic and pseudo-incompressible schemes by the potential temperature field (cf. equations (5.8)) $\theta(x, z, 0)$ shown (right).

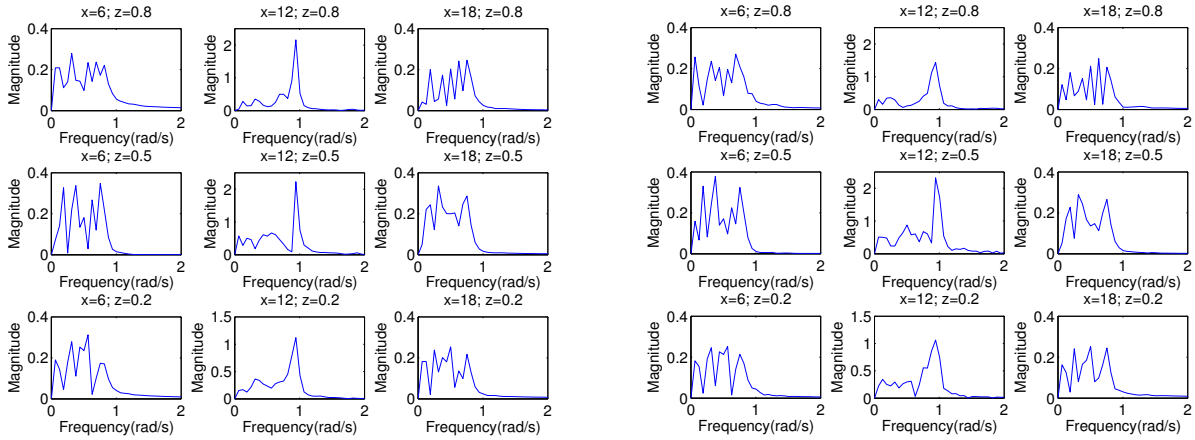

Figure 5.3: Boussinesq scheme: frequency spectra for regular (left block) and irregular (right block) meshes determined on various points in the domain $\mathcal{D}$. The position in the panel indicates the corresponding position in $\mathcal{D}$, for instance the upper left panel corresponds to a point at the upper left of $\mathcal{D}$.

The resulting spectra are presented in Figure 5.3. For all selected sample points, these spectra show an anisotropy manifested by the fact that they are bound from above by $N_b = 1/\mathrm{s}$. For the central point, the spectrum is pronounced for values of N_b, in well agreement with equations (5.2): for waves with frequency near N_b, the group velocity tends to zero leaving the corresponding waves trapped in the center of the domain. A very similar distribution of frequency spectra within the domain $\mathcal{D}$ has been found by [7]. The simulations on irregular meshes give very similar frequency spectra.

Figure 5.4 shows for regular (left column) and irregular (right column) meshes snapshots of the buoyancy field $b(x, z, t)$ at times $t = 5\,\mathrm{s}$ and $t = 8\,\mathrm{s}$ for a region $[11\,\mathrm{m}, 13\,\mathrm{m}] \times [0, 1\,\mathrm{m}]$. For these early times, before waves that are reflected by the boundaries reach the center, one clearly observes the internal gravity waves, caused by the buoyancy perturbation, that propagate from the center along the channel in x-direction. Besides of small irregularities of the solutions on irregular meshes, in particular visible at the velocity field that is not completely symmetric with respect to the axis $x = 10\,\mathrm{m}$, the results obtained either on regular or irregular meshes are very similar.

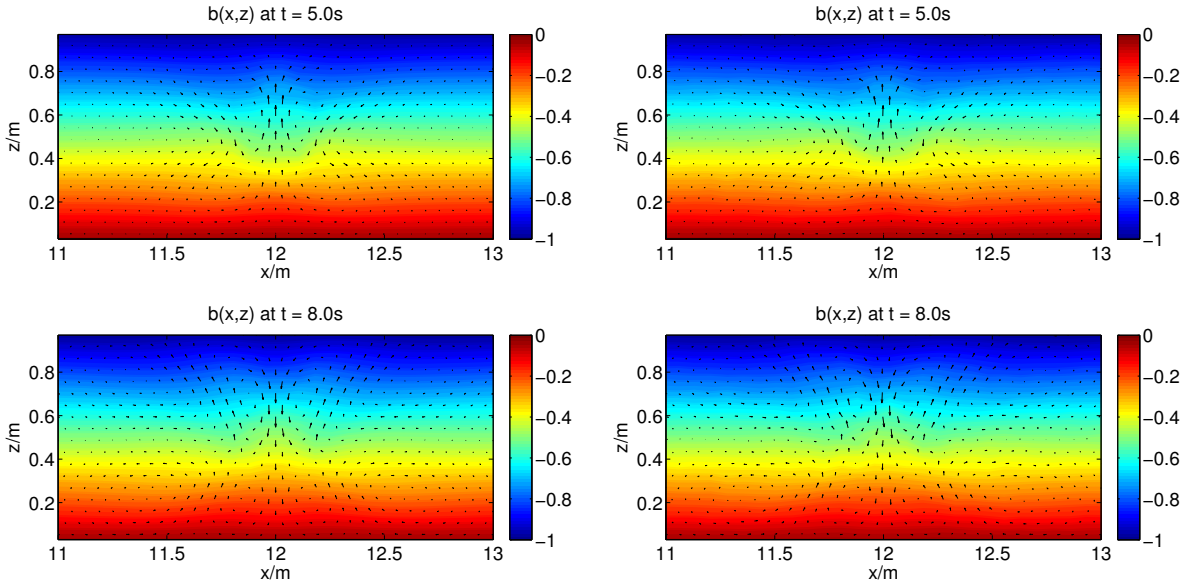

Figure 5.4: Boussinesq scheme: snapshots of the wave propagation on regular (left column) and irregular (right column) meshes.

Figure 5.5 illustrates for regular (left column) and irregular (right column) meshes the time evolution of the relative errors (determined as ratio of current values at t over initial value at $t = 0$) of total energy $E_{tot}(t)$ (upper panels) and mass $M(t)$ of equations (5.3) (lower panels). The middle panels show the energy transfer between kinetic $E_k(t)$ and potential $E_p(t)$ energy such that the sum of both energy sources, $E_{tot}(t)$, is conserved. One realizes that the initial surplus of potential energy, caused by the superimposed disturbance on the equilibrium state, triggers an oscillatory transfer between both energy sources.

As one can further deduce from these plots, the total energy shows an oscillatory behavior while being very well conserved in the mean for long integration times. Being symplectic, our variational integrator hence fulfills the expected behavior. The magnitude of oscillation is in the order of 10^{-6}, but depends on the time step size; here we used $\Delta t = 0.25\,\mathrm{s}$. Reducing the time step size by a factor of 10 decreases simultaneously the magnitude of the relative errors in total, kinetic, and potential energy by the same factor (not shown). Hence, our scheme shows the expected 1st-order convergence rate with time (cf. time scheme derivation in [26]). The mass $M(t)$ is conserved with an order of 10^{-15}. The quantities of interest for the simulations on irregular meshes are equally well conserved as on regular meshes.

5.1.2 Hydrostatic adjustment of the anelastic model

We consider the anelastic equations in hydrostatic equilibrium. By assuming that the reference states $\bar{\rho}(z)$ and $\bar{\theta}(z)$ are such that

$$N^2 = \frac{g}{\bar{\theta}}\frac{d\bar{\theta}}{dz} \quad \text{and} \quad \sigma_\mathrm{a} = \frac{1}{4}\left(\frac{1}{\bar{\rho}}\frac{d\bar{\rho}}{dz}\right)^2 - \frac{1}{2}\frac{d}{dz}\left(\frac{1}{\bar{\rho}}\frac{d\bar{\rho}}{dz}\right) \tag{5.5}$$

are constant numbers, the dispersion relation takes the simple form

$$\omega^2 = \frac{N^2 k_x^2}{\mathbf{k}^2 + \sigma_a}. \tag{5.6}$$

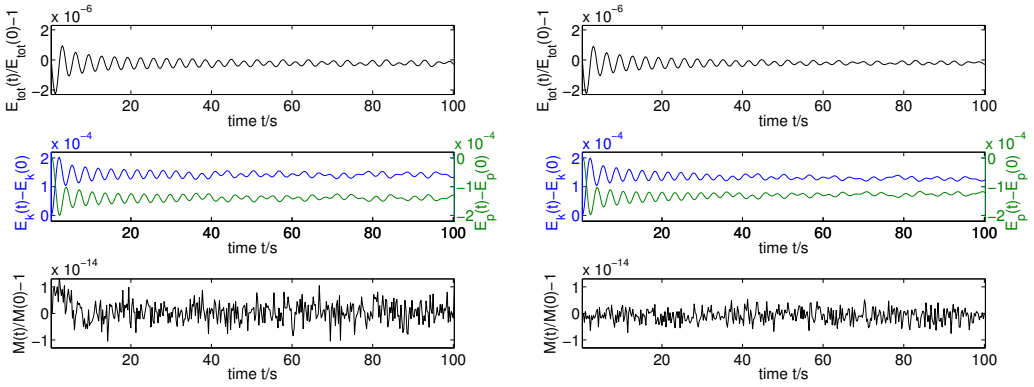

Figure 5.5: Boussinesq scheme: relative errors of total energy $E_{tot}(t)$ and mass $M(t)$, and energy transfer between kinetic $E_k(t)$ and potential $E_p(t)$ energy, for regular (left block) and irregular (right block) meshes.

Constant values for N and σ_a are obtained by taking $\bar{\theta}(z) = \alpha e^{\frac{N^2}{g}z}$ and $\bar{\rho}(z) = \beta e^{Kz}$, in which case $\sigma_a = \frac{K^2}{4}$.

Analogously to equations (5.2), also this dispersion relation shows an anisotropic spectra that is bound from above by N. To see this, consider the extremes of (5.6): the lower bound at $\min(\omega) = 0$ results from $k_x = 0$ while the upper bound $\max(\omega) = N$ results for $k_x \gg k_y, \sigma$.

For the anelastic equations, mass conservation is given by

$$\frac{d}{dt}\int_{\mathcal{D}} \bar{\rho}(z)\theta(x,z,t)d\mathbf{x} = 0, \tag{5.7}$$

as $\int_{\mathcal{D}} \bar{\rho}\partial_t\theta d\mathbf{x} = -\int_{\mathcal{D}} \mathbf{d}\theta \cdot \bar{\rho}\mathbf{u}d\mathbf{x} = -\int_{\mathcal{D}} \mathrm{div}(\bar{\rho}\mathbf{u}\theta)d\mathbf{x} + \int_{\mathcal{D}} \mathrm{div}(\bar{\rho}\mathbf{u})\theta d\mathbf{x} = 0$, which follows by the anelastic constraint $\mathrm{div}(\bar{\rho}\mathbf{u}) = 0$ and by the choice of boundary conditions, i.e. $\mathbf{u}\cdot\mathbf{n} = 0$, on $\partial\mathcal{D}$. We study if our anelastic discretization scheme conserves the latter quantity and if the total discrete energy, a discrete version of $E = \bar{\rho}\left(\frac{1}{2}|\mathbf{u}|^2 + c_p\bar{\pi}\theta\right)$ is well conserved, too.

Initialization. We aim for an initialization that produces results comparable to the Boussinesq scheme and that meets the requirements of constant N and σ_a in equations (5.5). To this end, the hydrostatic equilibrium is set up by $u_{\mathrm{eq}}(x,z) = w_{\mathrm{eq}}(x,z) = 0$ and a reference state $\bar{\theta}(z) = e^{z+c}$ for a constant c, on which at $t = 0$ a negative potential temperature perturbation $\tilde{\theta}(x,z)$ is superimposed. The initial potential temperature field $\theta(x,z,0) = \bar{\theta}(z) + \tilde{\theta}(x,z)$ in units $[\theta] = K$ is hence given by

$$\theta(x,z,0) = \begin{cases} e^{z+c} - \beta_a e^{\left(\frac{-r_0^2}{r_0^2 - r^2}\right)} & \text{if } r < r_0, \quad r^2 = (x - \frac{L_x}{2})^2 + (z - \frac{L_z}{2})^2, \\ e^{z+c} & \text{if } r \geq r_0, \end{cases} \tag{5.8}$$

with parameters $r_0 = 0.2 \cdot L_z$ and $\beta_a = 0.2 \cdot L_z$.

To obtain a potential temperature field with comparable magnitude (in the order of $\theta_0 = 1\,\mathrm{K}$) to the buoyancy field – but now with increasing value with height z as it would be in the atmosphere – we set $c = -L_z = -1$ (corresponding to $\alpha = 1/e$ from above) giving 0.4 K at the bottom and 1 K at the top of the domain. Note that β_a is slightly smaller than β_b of equations (5.4); it is chosen such that at the domain center x_c, z_c, there is $\theta(x_c, z_c, 0) \approx -b(x_c, z_c, 0)$ which results in similar magnitudes of oscillation. With this choice of θ, the Brunt-Väisälä frequency

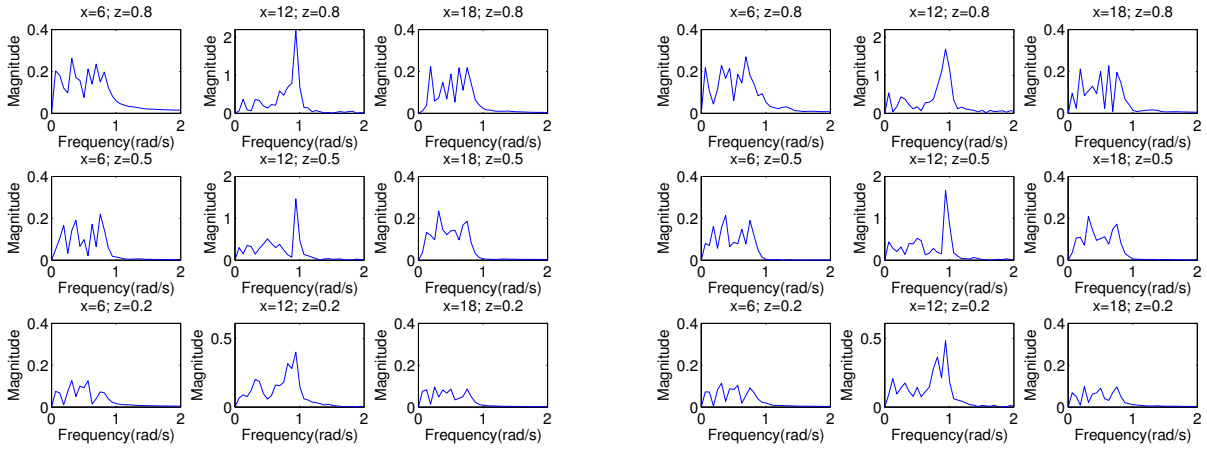

Figure 5.6: Anelastic scheme: frequency spectra for initialization (i) with $\bar{\rho}(z) = e^{-z}$ for regular (left block) and irregular (right block) meshes determined on various points in the domain $\mathcal{D}$ similarly to Fig. 5.3.

is $N^2 = \frac{g}{\bar{\theta}} \frac{d\bar{\theta}}{dz} = 1/\mathrm{s}^2$, where we set $g = 1\,\mathrm{m/s}^2$. This setup will allow us to compare the results obtained by the anelastic with those of the Boussinesq scheme from above and with those in [7].

The requirement that σ_a is constant, restricts our choice of the stratified density field $\bar{\rho}$ to be either a constant or an exponential function. We study our scheme using two profiles: (i) $\bar{\rho}(z) = e^{-z}$, which is very similar to a realistic stratification, and (ii) $\bar{\rho}(z) = e^{-8z}$ providing a very strongly stratified density field. To remain concise, we only present the frequency spectra for both profiles, while we restrict our representation elsewhere to the realistic profile and only comment on results obtained when using the strong density stratification.

The relation between $\bar{\pi}$ and $\bar{\theta}$ allows us to initialize the Exner pressure by the potential temperature field via

$$\bar{\pi}(z) = \frac{g}{c_p} e^{-(z+c)}\,. \tag{5.9}$$

for any values of specific heat at constant pressure c_p (here we set $c_p = 1$), as it will cancel out in the anelastic equations.

Given these functions, the discrete ones are obtained by setting $\Theta_i(0) = \theta(x_i, z_i, 0)$, $\bar{\Pi}_i = \bar{\pi}(x_i, z_i)$ and $\bar{\rho}_i = \bar{\rho}(x_i, z_i)$ for all triangles T_i with cell centers at position (x_i, z_i).

Results. Similarly to the Boussinesq scheme, we determine the frequency spectra by taking Fourier transforms of a time series of the potential temperature field $\theta(x, z, t)$ for the time interval $t = [0, 100\,\mathrm{s}]$ at locations in $\mathcal{D}$ similar to those in Section 5.1.1. Figure 5.6 shows the various frequency spectra for initialization (i) $\bar{\rho}(z) = e^{-z}$; left block for the regular, and right block for the irregular meshes. These spectra consist of frequencies lying between zero and $\max(\omega) = N = 1/\mathrm{s}$, which agrees well with the frequency pattern in Figure 5.3 and reflects very well the properties of the analytical dispersion relation (5.6).

Using strong stratification (density initialization (ii) $\bar{\rho}(z) = e^{-8z}$), the spectra shown in Figure 5.7 for both mesh types are similar to Figure 5.6, in particular their lower and upper boundaries. The distribution of occupied wave numbers though slightly differs from initialization (i): the upper panels show in general higher magnitude, the central panels show increased

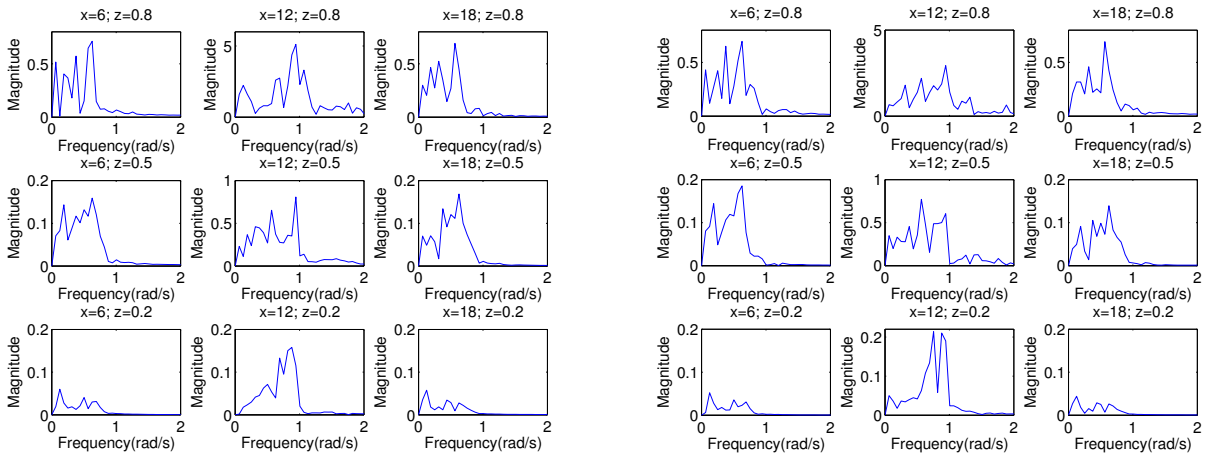

Figure 5.7: Anelastic scheme: frequency spectra for initialization (i) with $\bar{\rho}(z) = e^{-8z}$ for regular (left block) and irregular (right block) meshes determined on various points in the domain $\mathcal{D}$ similarly to Figure 5.3. The spectra of the pseudo-incompressible scheme using this initialization show very similar pattern (not shown).

magnitude of small wave numbers, while the peaks at $N = 1/\mathrm{s}$ are not as distinct as for the weaker density stratification. In case of strong stratification, the magnitudes of oscillation are strongest at the upper boundary, i.e. in the region with lowest density. This causes small scale waves (noise) that are distributed over the domain and that occupy the small waves numbers in the spectra.

In Figure 5.8, we show snapshots of the potential temperature $\theta(x, z, t)$ at time $t = 5\,\mathrm{s}$ and $t = 8\,\mathrm{s}$ for the region $[11\,\mathrm{m}, 13\,\mathrm{m}] \times [0, 1\,\mathrm{m}]$ using the realistic density profile (i). Comparing with Figure 5.4, the velocity and potential temperature fields for both time instances and both mesh types are rather similar to those obtained with the Boussinesq scheme, noticing that the magnitude of displacement of θ from equilibrium is more enhanced in the anelastic case. Again, the irregular meshes (right column) trigger solutions that are slightly non axis-symmetric with respect to $x = 10\,\mathrm{m}$, but agree in general very well with the internal gravity wave propagations obtained on regular meshes.

Figure 5.9 shows the relative errors of total energy (upper panels) and mass of equations (5.7) (lower panels) for regular (left column) and irregular (right column) meshes. Again, the central panels show the energy transfer between kinetic and potential energy. In all cases, these quantities are as well conserved as for the Boussinesq scheme, in particular their mean is very well conserved for long integration times. The conservation of mass shows a slight growth (in particular for the irregular mesh), but within the order of 10^{-13} on a very acceptable level. For these plots we used a time step size of $\Delta t = 0.25\,\mathrm{s}$. Similar to above, the anelastic scheme shows the expected 1st-order convergence rate with time (cf. Section 5.1.1 for more details).

Remark 5.1 By setting $\bar{\rho} = \rho_0$ and $\bar{\theta} = \theta_0$ as constants, the analytical Boussinesq and anelastic models agree. By initializing the discrete schemes in equations (4.7) and (4.11) accordingly, i.e. by setting $\theta = -b$, $\bar{\rho} = 1$, $\bar{\theta} = \theta_0 = 1$, and $c_p = 1$, we could exactly recover the numerical results of the Boussinesq by the anelastic scheme (not shown).

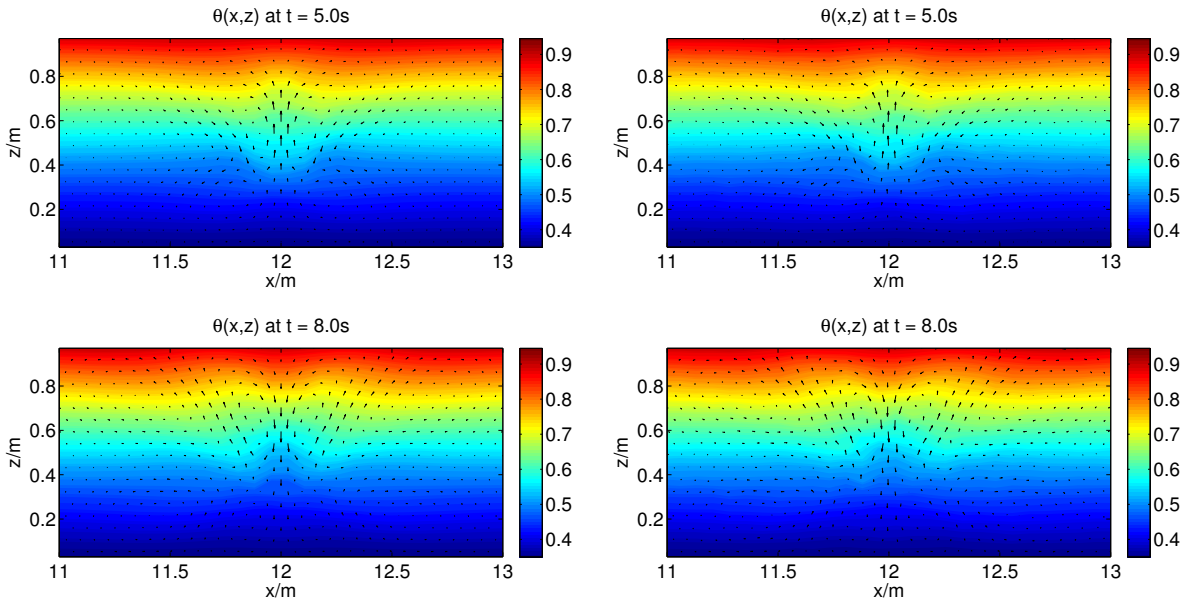

Figure 5.8: Anelastic scheme: snapshots of the wave propagation on regular (left column) and irregular (right column) meshes for $\bar{\rho}(z) = e^{-z}$

5.1.3 Hydrostatic adjustment of the pseudo-incompressible model

We consider the pseudo-incompressible equations in hydrostatic equilibrium. By assuming that the reference states $\bar{\rho}(z)$ and $\bar{\theta}(z)$ are such that

$$N^2 = \frac{g}{\bar{\theta}}\frac{d\bar{\theta}}{dz} \quad \text{and} \quad \sigma_{\text{pi}} = \left(\frac{1}{\bar{\theta}}\frac{d\bar{\theta}}{dz} + \frac{1}{2\bar{\rho}}\frac{d\bar{\rho}}{dz}\right)^2 - \frac{d}{dz}\left(\frac{1}{\bar{\theta}}\frac{d\bar{\theta}}{dz} + \frac{1}{2\bar{\rho}}\frac{d\bar{\rho}}{dz}\right) \tag{5.10}$$

are constant numbers, the dispersion relation takes the simple form

$$\omega^2 = \frac{N^2 k_x^2}{\mathbf{k}^2 + \sigma_{\text{pi}}}. \tag{5.11}$$

Therefore, the dispersion relation (5.11) is anisotropic and bound from above by $\max(\omega) = N$ just as for the Boussinesq and anelastic models, which results from the same reasoning as done for equation (5.6).

For the pseudo-incompressible equations, we note that the mass conservation is given by

$$\frac{d}{dt}\int_{\mathcal{D}} \bar{\rho}(z)\bar{\theta}(z)\theta(x,z,t)d\mathbf{x} = 0, \tag{5.12}$$

which follows by a similar argumentation as presented for equation (5.7). Moreover, we study if the total discrete energy that corresponds to the energy density $E = \bar{\rho}\bar{\theta}/\theta\left(\frac{1}{2}|\mathbf{u}|^2 + gz\right)$ is well conserved.

Initialization. The pseudo-incompressible scheme is initialized exactly as the anelastic scheme with the only difference that here we do not need to define the Exner pressure $\bar{\pi}(z)$ (cf. equation (4.15)). In particular, by choosing exponential functions for the potential temperature and the density fields, that is $\bar{\theta}(z) = e^z$ and (i) $\bar{\rho}(z) = e^{-z}$ or (ii) $\bar{\rho}(z) = e^{-8z}$, we guarantee that

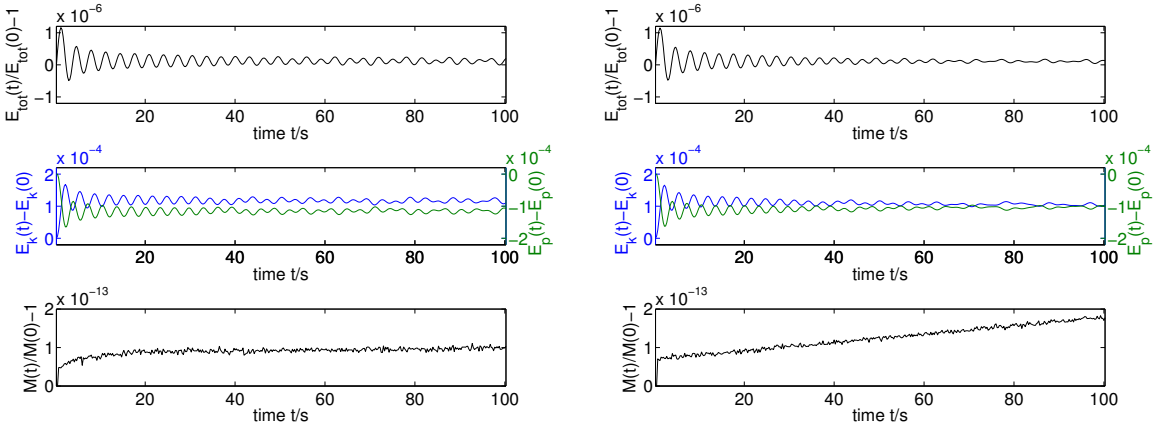

Figure 5.9: Anelastic scheme: relative errors of total energy $E_{tot}(t)$ and mass $M(t)$, and energy transfer between kinetic $E_k(t)$ and potential $E_p(t)$ energy, for regular (left block) and irregular (right block) meshes.

the conditions put on N and σ_{pi} to be constant, required to be able to calculate the dispersion relation (5.11), are fulfilled. As above, we study the dynamics, the conservation of the quantities of interest, and the dispersion relations for the two different density stratifications (i) and (ii).

Results. Analogously to Section 5.1.2, we determine the frequency spectra by taking Fourier transforms of a time series of $\theta(x, z, t)$ for the time interval $t = [0, 100\,\text{s}]$ at various locations in $\mathcal{D}$. Figure 5.10 shows the resulting frequency spectra for initialization (i) $\bar{\rho}(z) = e^{-z}$; left block for the regular, and right block for the irregular mesh. For both regular and irregular meshes, these spectra show a very similar pattern as in Figure 5.6, in particular a sharp drop in the spectra at the maximal frequencies $\max(\omega) = 1/\text{s}$ as theoretically expected. When using initialization (ii), the spectra for both regular and irregular meshes are similar to those presented in Figure 5.7 for the anelastic case; one observes also here an increase of small wave numbers occupying the frequency spectra, in particular on the upper panels (not shown).

In Figure 5.11, we show snapshots of the potential temperature $\theta(x, z, t)$ at time $t = 5\,\text{s}$ and $t = 8\,\text{s}$ for a region $[11\,\text{m}, 13\,\text{m}] \times [0, 1\,\text{m}]$ and for the density profile (i). They show for both time instances and both mesh types very similar dynamical behavior as for Boussinesq and anelastic cases.

Figure 5.12 shows the relative errors of total energy and mass of equation (5.12) and the energy transfer between kinetic and potential energy. On both mesh types, the errors are in the same order as for the Boussinesq and anelastic schemes. Also here, the time step size is $\Delta t = 0.25\,\text{s}$ and the scheme shows the expected 1st-order convergence rate with time. The time evolution of mass shows a slight decline, but only in the order of 10^{-14}, hence it is very well conserved.

5.2 Kelvin-Helmholtz instability

In this section, we show for all soundproof variational integrators that they correctly capture the Kelvin Helmholtz instability (KHI). In literature, KHI is mostly studied with models assuming the Boussinesq approximation. Considering Remark 5.1, here we include in our studies also the anelastic, and similarly also the pseudo-incompressible models.

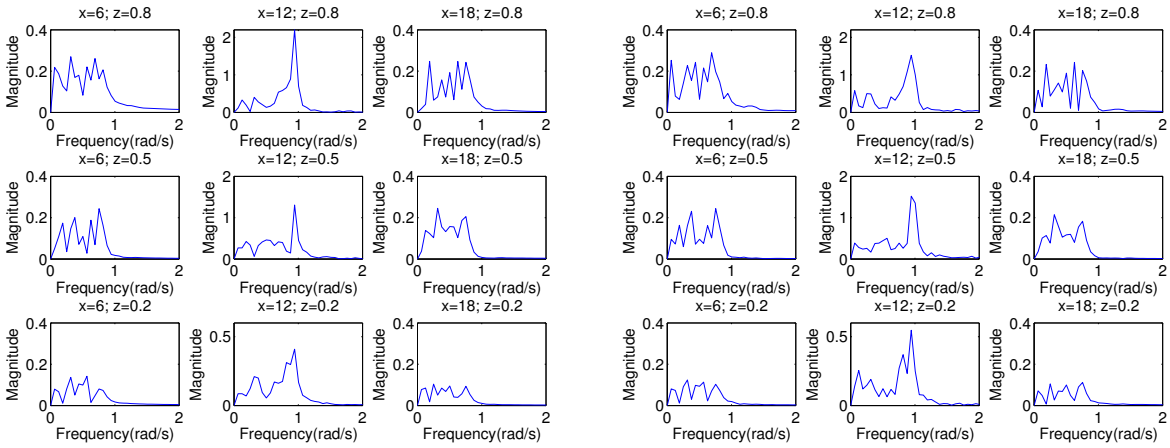

Figure 5.10: Pseudo-incompressible scheme: frequency spectra for initialization (i) with $\bar{\rho}(z) = e^{-z}$ for regular (left block) and irregular (right block) meshes determined on various points in the domain $\mathcal{D}$ similarly to Figure 5.3.

Considering a stratified horizontal shear flow with stabilizing density stratifications, KHI may occur if the flow parameters are such that the Richardson number J (see definition below) is less than 0.25 [8]. For values of J above, the flow is stable. We study in the following if our schemes correctly represent this stability threshold.

Initialization. We use a computational domain of $(x, z) \in [0, L_x] \times [0, L_z], L_x = 20\,\mathrm{m}, L_z = 10\,\mathrm{m}$, with periodic boundary conditions in x-direction and free-slip boundary conditions in z-direction. We use for all simulations a time step size of $\Delta t = 0.05\,\mathrm{s}$ and apply regular meshes with a resolution of $2 \cdot 214 \times 124$ triangular cells.

The initial wind field is taken as a horizontal flow that advects the buoyancy field b, respectively the potential temperature field θ on which a vertical disturbance is superimposed. In more detail, the horizontal velocity field with the characteristic scale of length $d \in \mathbb{R}$ is given by

$$u(x, z, 0) = U_0 \tanh\left(\frac{z}{d}\right) \text{ for } z \in [0, L_z]. \tag{5.13}$$

In order to trigger the KHI, we disturb the horizontal velocity field by a small vertical disturbance, given by

$$w'(x, z, 0) = \mathrm{Real}\{w(z)e^{ik(x-ct)}\}\,, \tag{5.14}$$

where k and c describe the horizontal wave number and the phase velocity of the disturbance, respectively. $w(z)$ is a nontrivial solution of the Taylor-Goldstein equation, describing the vertical structure of a neutral mode; for $s := \tanh\left(\frac{z}{d}\right)$ and some constant A, it is given by

$$w(z) = \begin{cases} As^{(1-\hat{k}^2)}\left(1-s^2\right)^{\frac{\hat{k}^2}{2}} & \text{for } s > 0, \\ A|s|^{(1-\hat{k}^2)}\left(1-|s|^2\right)^{\frac{\hat{k}^2}{2}} e^{-i\pi(1-\hat{k}^2)} & \text{for } s < 0, \end{cases} \tag{5.15}$$

(as for $s < 0, s = |s|e^{-i\pi}$), where $\hat{k} = kd$ holds. We refer to [21, 20] for more details on the derivation of this mode.

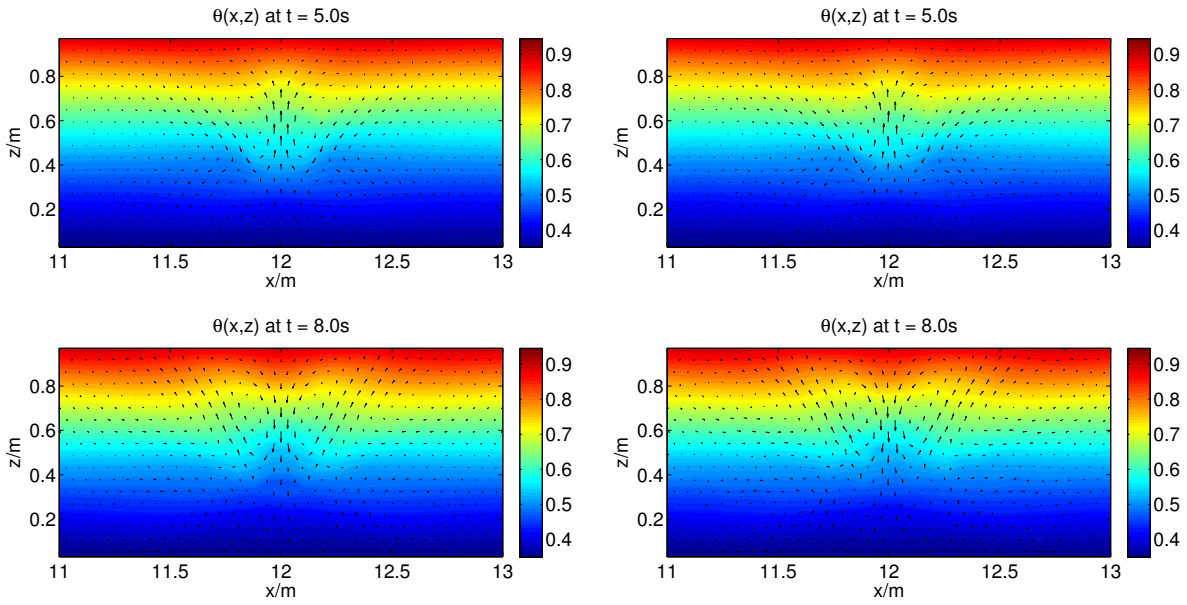

Figure 5.11: Pseudo-incompressible scheme: snapshots of the wave propagation on regular (left column) and irregular (right column) meshes for $\bar{\rho}(z) = e^{-z}$.

The condition required for instability can be represented by the Richardson number:

$$J = \frac{N^2}{\left(\frac{du}{dz}\right)^2} = \frac{N^2 d^2}{U_0^2}\,, \tag{5.16}$$

in which N is the Brunt-Väsälä frequency of either Eqns (5.2) or (5.6). Given J, the neutral mode (5.15) requires $J_\mathrm{n} = 1/4$ and the relation $J_\mathrm{n} = \hat{k}^2(1-\hat{k}^2)$ holds (cf. Drazin [8]). Hence, we find for the horizontal wave number: $k = \frac{2\pi n}{L_x}$ with $n = \frac{L_x}{\lambda} \in \mathbb{Z}\backslash 0$. Moreover, for $J_\mathrm{n} = 0.25$ there is $k^2 d^2 = 0.5$ and hence $d = \frac{\sqrt{0.5}L_x}{2\pi n}$. With this setup, there follows that in case of $J < J_\mathrm{n}$ the flow is in the unstable regime, and for $J \geq J_\mathrm{n}$ in the stable one (cf. curve of neutral stability of Drazin [8]).

Initial fields for Boussinesq scheme. The buoyancy in case of the Boussinesq scheme is initialized by the function $b(x,z,0) = \bar{b}(z) = -N^2 z$ with Brunt-Väsälä frequency $N = 1/\mathrm{s}$, i.e. we use the unperturbed function of Sect. 5.1 in which $\beta_b = 0$ (cf. Fig. 5.13). Here, no density field has to be initialized.

As flow parameters, we use $n = 2$ and $A = 0.05 \cdot U_0$ as magnitude of disturbance, while setting: i) $U_0 = 1.8\,\mathrm{m/s}$ to obtain $J = 0.40$, and ii) $U_0 = 3.5\,\mathrm{m/s}$ to obtain $J = 0.10$.

Initial fields for anelastic and pseudo-incompressible schemes. To obtain a similar stratification as in the Boussinesq case, we initialize the anelastic and pseudo-incompressible schemes by the potential temperature $\theta(x,z,0) = \bar{\theta}(z) = L_z e^{(z-L_z)/L_z}$ (cf. Fig. 5.13), with corresponding Exner pressure $\bar{\pi}(z) = \frac{g}{c_p} e^{-(z-L_z)/L_z}$. This choice guarantees that the Brunt-Väsälä frequency N and hence also the Richardson number $J = \frac{N^2 d^2}{U_0^2 L_z}$ are constants (cf. Sect. 5.1.2). For the density stratifications, we apply several profiles; the results presented below are obtained using the density $\bar{\rho}(z) = e^{-z/L_z}$, a profile similar to that in Sect. 5.1.2, but the following

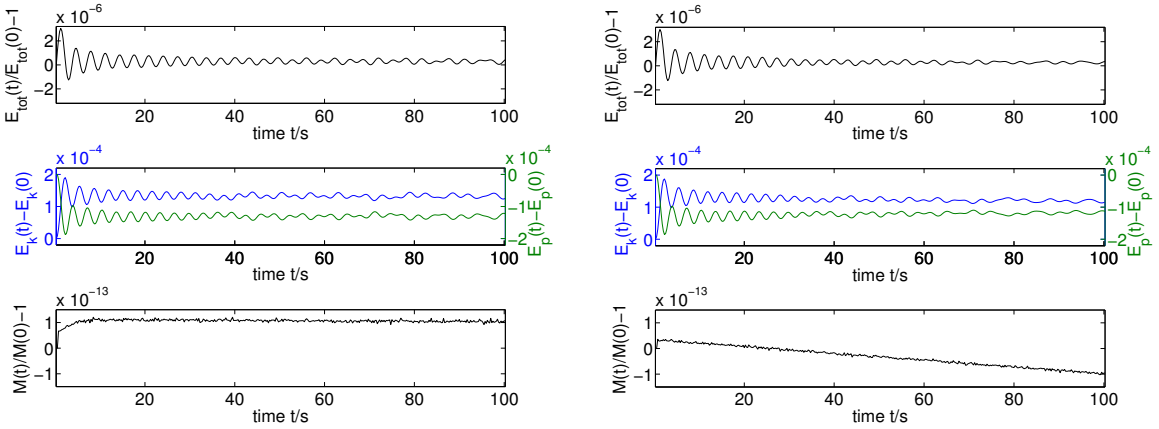

Figure 5.12: Pseudo-incompressible scheme: relative errors of total energy $E_{tot}(t)$ and mass $M(t)$, and energy transfer between kinetic $E_k(t)$ and potential $E_p(t)$ energy, for regular (left block) and irregular (right block) meshes.

results, in particular the regime of stability or instability, are valid too for a constant profile or the realistic one introduced in Eqn. (5.19).

As flow parameters, we use $n = 2$ and $A = 0.2 \cdot U_0$ for the settings: i) $U_0 = 0.56\,\mathrm{m/s}$ to obtain $J = 0.40$ and ii) $U_0 = 1.1\,\mathrm{m/s}$ to obtain $J = 0.10$.

Results. Figure 5.13 shows the buoyancy $b(x, z, t)$ of the Boussinesq scheme (upper panels) and the potential temperature $\theta(x, z, t)$ of the anelastic and pseudo-incompressible schemes (middle and lower panels) for two different Richardson numbers J: on the left $J = 0.4$ and on the right $J = 0.1$. For the Richardson number of $J = 0.4$, the flows of all schemes remain stable, as shown here for an integration time of 20 s. For $J = 0.1$, we observe for all schemes the development of KHI. The usage of irregular meshes or, in the case of the anelastic and pseudo-incompressible schemes different density profiles, does not alter these results. In particular, the flow structures of stable and unstable flow for either b or θ look very similar for all these cases (not shown).

From Figure 5.14 we deduce that, in the stable regimes, all three schemes preserve well the total energy. The corresponding energy plots indicate a slight trend during the first 20 s, but for much longer integrations (we tested up to 100 s (not shown)) they stabilize at the order of 10^{-7} while showing similar oscillation as in e.g. Figure 5.5. In the unstable regime, the total energy during the first 20 s is preserved at the order of about 10^{-5} for the Boussinesq, and 10^{-6} for the other schemes. For longer integration times, when the mixing between upper and lower flow layers develops such fine filaments that reach the limit of spatial resolution, our simulations gets more and more noise (not shown). Even in such an extreme case, our schemes preserve total energy at the order of about 10^{-3} for a simulation of up to 100 s although they are not constructed to represent such turbulent flow. Corresponding simulations on irregular meshes result in very similar accuracy behavior confirming the schemes' insensitivity on the shape of the grid cells. In all cases studied, mass (given by (5.3), (5.7), or (5.12)) is conserved at the order of machine precision (not shown).

Figure 5.14 shows, moreover, the energy transfer between kinetic $E_k(t)$ and potential energy $E_p(t)$. We realize that for all cases energy is entirely transfered between potential and kinetic energy sources such that the sum of both is conserved. Considering first the left panels in which

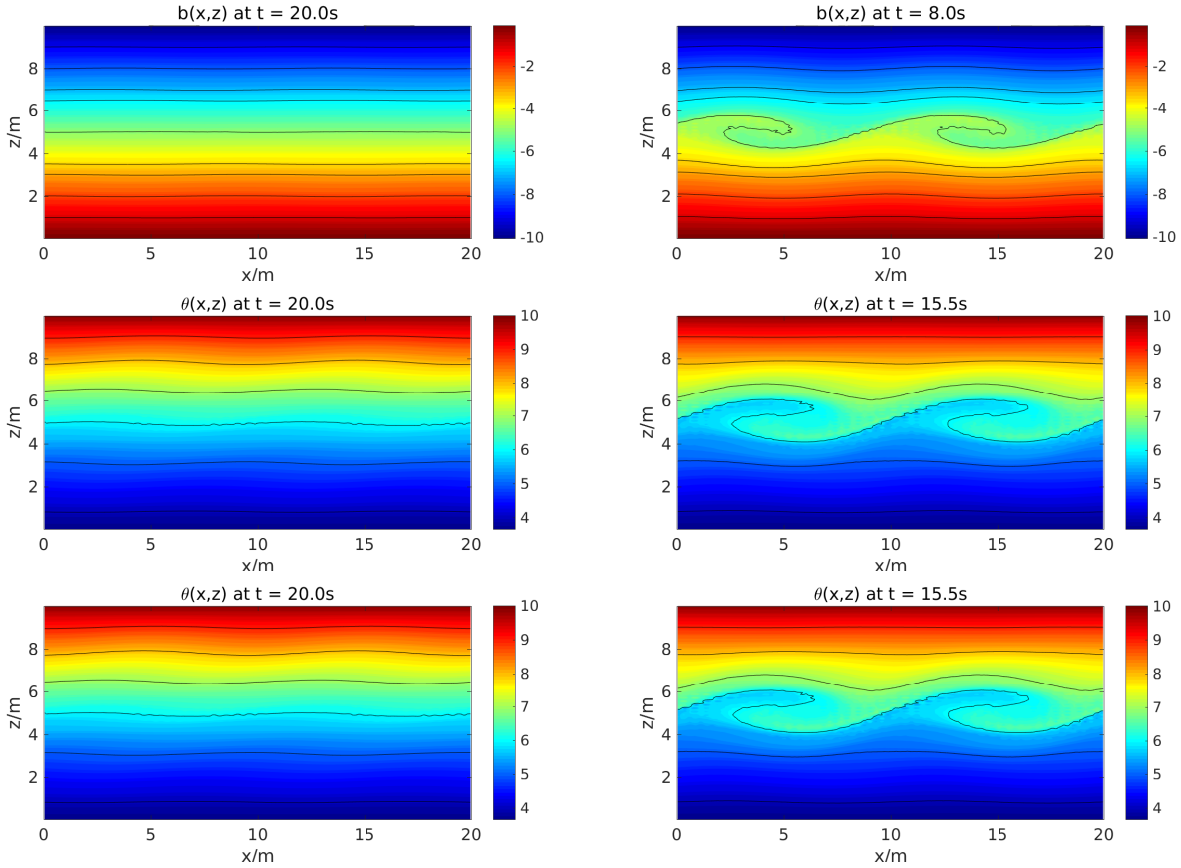

Figure 5.13: Buoyancy $b(x, z)$ of the Boussinesq (upper panels) and potential temperature $\theta(z, x)$ of the anelastic and pseudo-incompressible schemes (middle and lower panels) on regular meshes for two different Richardson numbers J: on the left $J = 0.4$ and on the right $J = 0.1$. Contour lines: for the upper panels $[0, -1, -2, -3, -3.5, -5, -6.5, -7, -8, -9, -10]$; for the middle and lower panels: $[4, 5, 6, 7, 8, 9, 10]$.

the flow is in a stable regime, the initial surplus of kinetic energy is transfered into potential energy with a peak of the latter for b at $t = 2.5\,\mathrm{s}$ and for θ at $t = 6\,\mathrm{s}$. However, most of this energy is transferred back into E_k leading to a stable stratification. In contrast on the right panels, the initial surplus of kinetic energy, which is at least one order of magnitude larger then in the stable regime, is sufficient to trigger the instability, lifting heavier particles over lighter ones which leads to an increase in potential energy. This effect can be clearly seen in the transfer of kinetic toward potential energy.

5.3 Rising and falling bubble test cases

On advection dominated test cases, namely (i) a rising hot bubble in a cold environment and (ii) a cold drop of air in a warm environment, we illustrate the dynamics of the anelastic and pseudo-incompressible schemes. We point out the similarities and differences between the underlying approximations and we test whether our variational integrators share these properties.

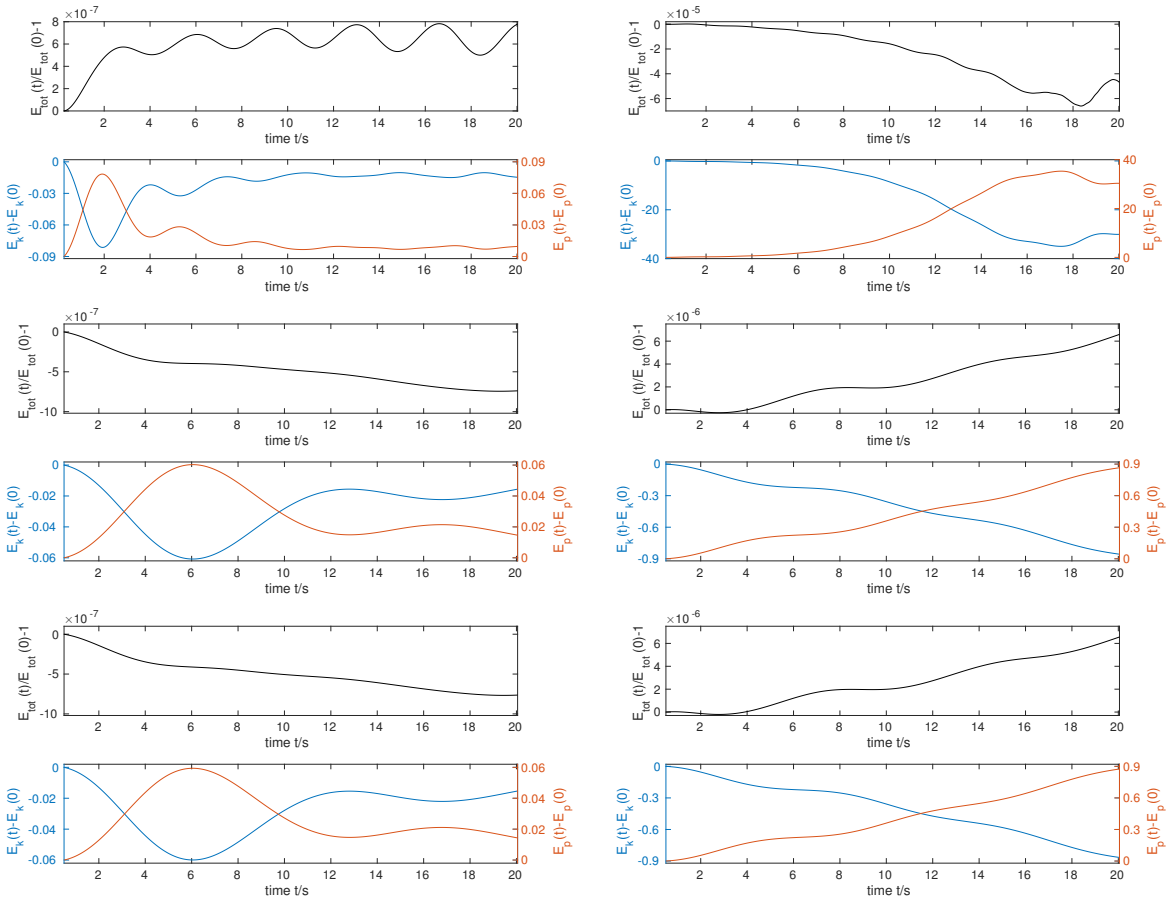

Figure 5.14: Relative error in total energy $E_{tot}(t)$ and energy transfer between kinetic $E_k(t)$ and potential $E_p(t)$ energy for the Boussinesq scheme (upper panels) and for the anelastic and pseudo-incompressible schemes (middle and lower panels) on regular meshes for two different Richardson numbers J: on the left $J = 0.4$ and on the right $J = 0.1$.

5.3.1 Rising bubble test cases

Using the test case of a rising hot bubble of air in a cold environment, we will verify in the following that in case of small potential temperature variations, the anelastic and pseudo-incompressible schemes behave very similarly. In order to enable quantitative comparisons also with literature, we set up the test case similarly to [17].

Initialization. We use a domain of dimension $(x, z) \in [0, L_x] \times [0, L_z], L_x = 20\,\text{km}, L_z = 10\,\text{km}$, with periodic boundary condition in x-direction and free-slip boundary conditions at the upper and lower boundaries of the domain. The regular and irregular meshes have a resolution of $2 \cdot 321 \times 186$ cells and we use a time step size of $\Delta t = 2.5\,\text{s}$.

The potential temperature distribution consisting of a constant background state $\bar{\theta} = 300\,\text{K}$ and some initial disturbance $\theta'(x, z, 0)$ is given by

$$\theta(x, z, 0) = 300\,\text{K} + \begin{cases} \delta\theta \cos^2\left(\frac{\pi}{2} r\right) & \text{for } r \leq 1,\ r = 5\sqrt{\left(\frac{x - \frac{1}{2}L_x}{L}\right)^2 + \left(\frac{z - \frac{1}{2}L_z}{L} + z_{\text{off}}\right)^2}, \\ 0 & \text{otherwise,} \end{cases} \tag{5.17}$$

with values for $\delta\theta = 2\,\text{K}$, $L = 10\,\text{km}$, and $z_{\text{off}} = 0.03\,L$. This results in an Exner pressure $\bar{\pi}(z) = -\frac{g}{c_p \bar{\theta}} z$ with $\bar{\pi}(z = 0) = 0$.

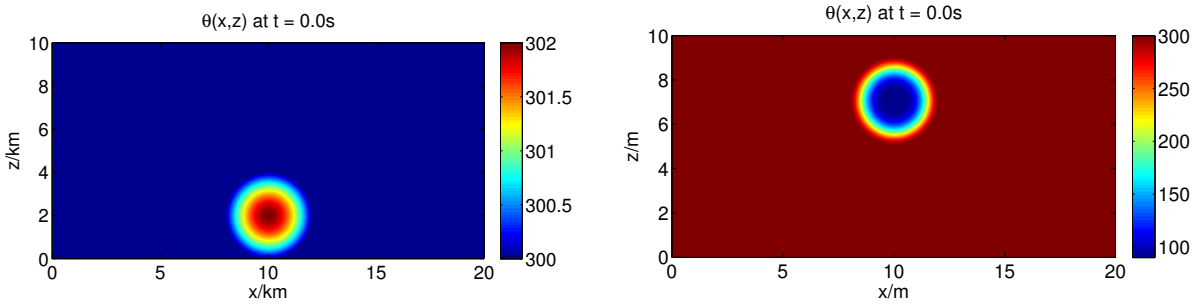

Figure 5.15: Initial conditions: on the left for the warm bubble test case, on the right for the cold bubble test case with $\delta\theta = 210\,\mathrm{K}$ (cf. Section 5.3.2).

The hydrostatic background density stratification shall be described by (cf. [25])

$$\bar{\rho}(\hat{z}) = \frac{P_{ref}}{R\bar{\theta}}\left(1 - \beta\hat{z}\right)^{\frac{1}{\gamma-1}}, \qquad \beta = \frac{gL_z}{c_p\bar{\theta}}, \qquad \hat{z} = \frac{z}{L_z}, \tag{5.18}$$

$$\bar{\rho}(z) = \left(1 - 0.3\frac{z}{L_z}\right)^{\frac{5}{2}}, \quad \text{for } z \in [0, L_z]. \tag{5.19}$$

For the parameters, we have chosen typical values for a dry atmosphere: isentropic exponent $\gamma = 1.4$, specific heat of $c_p = 1000\,\frac{\mathrm{J}}{\mathrm{K\,kg}}$, gas constant of $R = 287\,\frac{\mathrm{J}}{\mathrm{K\,kg}}$, a reference pressure of $P_{ref} = 10^5\,\frac{\mathrm{kg}}{\mathrm{m\,s^2}}$ and a gravitational acceleration of $g = 10\,\frac{\mathrm{m}}{\mathrm{s^2}}$; leading to $\beta \approx 0.3$ and $\frac{P_{ref}}{R\bar{\theta}} \approx 1$. For $z = 0$, equation (5.19) gives $\bar{\rho}(z=0) = 1\,\frac{\mathrm{kg}}{\mathrm{m\,s^2}}$ (in agreement with [17]). Using this analytical functions we initialize the discrete ones as described above.

Using this initialization, we expect to obtain results very similar to those of Klein [17]. As the integration time with 1000 s is such that the bubble does not interact with the boundaries and as the initialization is axis-symmetric to $x_c = 10\,\mathrm{km}$ (cf. Figure 5.15), the difference in the choice of boundary conditions for our setup and that in [17] does not influence the results.

Results. Figure 5.16 shows the potential temperature $\theta(x, z, t)$ for the anelastic (left column) and pseudo-incompressible schemes (right column) for regular (upper row) and irregular (lower row) meshes after an integration of 1000 s. The initial data are symmetric with respect to vertical axis $x_c = 10\,\mathrm{km}$. As the initial maximum of potential temperature is located on this symmetry line and as the boundary conditions are mirror-symmetric too, the maximum value should stay on the symmetric line and it's value should be conserved during the integration.

Choosing the initialization of Klein [17], we are able to directly compare the results. First we note that the results for the anelastic and pseudo-incompressible schemes under small variations in potential temperature (i.e. $\theta_{max}/\theta_{min} = 302\,\mathrm{K}/300\,\mathrm{K}$) are almost indistinguishable, in agreement with [17]. This is true for both regular and irregular meshes. Moreover, both schemes present well the advection speed of the bubbles reaching a height of 8 km after an integration of 1000 s, in well agreement with literature.

As to the symmetry of the solutions, anelastic and pseudo-incompressible schemes on regular meshes show nicely the required symmetry behavior while the maxima stay indeed on the symmetry line, but increases to $\theta_{\max} = 2.5\,\mathrm{K}$. This is in contrast to [17], in which the solution develops two local extrema located symmetrically some finite distance away from the symmetry line while the maximal value of θ reaches, in their best case simulations, $\theta_{\max} = 1.73K$. These

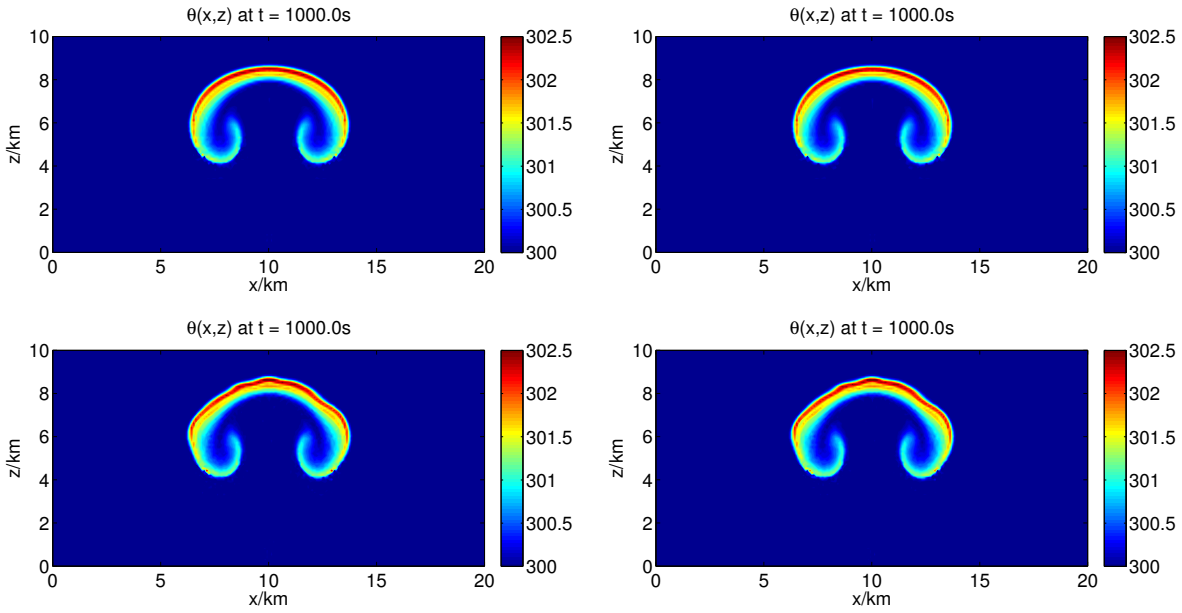

Figure 5.16: Potential temperature at $t = 1000\,\mathrm{s}$ for the anelastic (left column) and pseudo-incompressible schemes (right column) on regular (upper row) and irregular (lower row) meshes.

latter results had been obtained by using a scheme that applies flux limiters that avoid the development of too steep gradients of θ. As our schemes do not apply such flux limiters, or any kind of smoothing methods, such steep gradients develop, in particular for latter times when the bubble is strongly stretched, leading to the increased maximal potential temperature values.

Using irregular meshes for the variational anelasic and pseudo-incompressible schemes, the general dynamical behavior of the rising bubble and, in particular, the symmetry of the solutions are well represented. Only the shapes of the stretched bubbles show some wiggles that result from the distorted triangles on the irregular meshes. Here, the maximal values of potential temperature is about $\theta_{\max} = 2.8\,\mathrm{K}$.

From Figure 5.17 we deduce that for regular and irregular meshes both anelasic and pseudo-incompressible schemes conserve very well the total energy in the order of 10^{-6} and that, for each scheme, there is almost no difference of the results obtained on either regular or irregular meshes. For all cases, the mass as defined in equations (5.7) and (5.12) is conserved in the order of 10^{-14} (not shown).

5.3.2 Cold bubble test case

Finally we study the different behavior of the variational anelastic and pseudo-incompressible schemes in case of large potential temperature variations. Again, we set up the test case similarly to [17] which allow us to compare the results.

Initialization. The computational domain is given by $(x, z) \in [0, L_x] \times [0, L_z], L_x = 20\,\mathrm{m}, L_z = 10\,\mathrm{m}$, with periodic boundary condition in x-direction and free-slip boundary conditions in z-direction. Also here, we calculate on regular and irregular meshes with a resolution of $2 \cdot 321 \times 186$ triangles. We use a time step size of $\Delta t = 0.0125\,\mathrm{s}$.

The potential temperature distribution consisting of a constant background state $\bar{\theta} = 300\,\mathrm{K}$

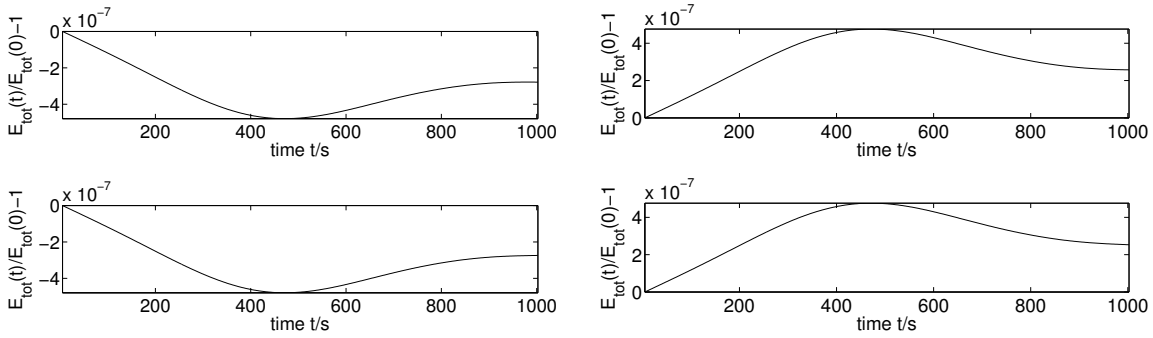

Figure 5.17: Relative error in total energy for the anelastic (left column) and pseudo-incompressible schemes (right column) for regular (upper row) and irregular meshes (lower row) for the warm bubble test case.

and some initial disturbance $\theta'(x, z, 0)$ is given by

$$\theta(x, z, 0) = 300\,\mathrm{K} - \begin{cases} \frac{\delta\theta}{2}(1+\cos(\pi r^2)) & \text{for } r \leq 1,\ r = 5\sqrt{\left(\frac{x-\frac{1}{2}L_x}{L}\right)^2+\left(\frac{z-\frac{1}{2}L_z}{L}+z_{\text{off}}\right)^2}, \\ 0 & \text{otherwise,} \end{cases} \tag{5.20}$$

with values for $\delta\theta = 30\,\mathrm{K}$ and $210\,\mathrm{K}$, $L = 10\,\mathrm{m}$, and $z_{\text{off}} = -0.02\,L$. The Exner pressure $\bar{\pi}(z)$ required for the anelastic, and the background density stratification $\bar{\rho}(z)$ required for both schemes are the same as in the warm bubble test case. Using this analytical functions we initialize the discrete ones as described above.

Analogously to the warm bubble case, by using this initialization we expect to obtain very similar results to those presented in Klein [17], as also for this test case the bubble does not interact with the boundaries and as the initialization is axis-symmetric to $x_c = 10\,\mathrm{m}$ (cf. Figure 5.15).

Results. Figure 5.18 shows the potential temperature fields of the falling cold air bubble with $\delta\theta = 30\,\mathrm{K}$ (upper row) and $\delta\theta = 210\,\mathrm{K}$ (lower row) for the anelastic (left column) and pseudo-incompressible schemes (right column) on regular meshes. We realize that for small potential density variations, the anelastic and pseudo-incompressible schemes give very similar results (upper row), as already verified above for the warm bubble test case. For larger density variations though, the corresponding potential temperature fields obviously differ (cf. lower row). The results obtained on irregular meshes are almost indistinguishable from those presented in Figure 5.18 (hence not shown).

The differences between the anelastic and pseudo-incompressible models are caused by the different pressure gradient terms, i.e by the, in time, linear term $\nabla(\bar{\theta}\pi)$ for the anelastic and by the nonlinear term $\theta\nabla\pi$ for the pseudo-incompressible models, as explained in the following. The shape of the bubble in the anelastic case (left column of Figure 5.18) is mainly cause by the horizontal variation of buoyancy force, with maximum value at the symmetry axis $x_c = 10\,\mathrm{m}$. There, the air is the heaviest and will fall the fastest, with decreasing values to either the right or left hand side. This gradient in fall velocity will cause negative vorticity on the right and positive vorticity on the left of x_c, stretching the initial round bubble into a thin sheet. This, so called, first baroclinic effect, which merely changes even in case of high potential temperature variations, causes the stretching of the bubble when it falls down and is the reason for the stretching of the bubble in the anelastic case.

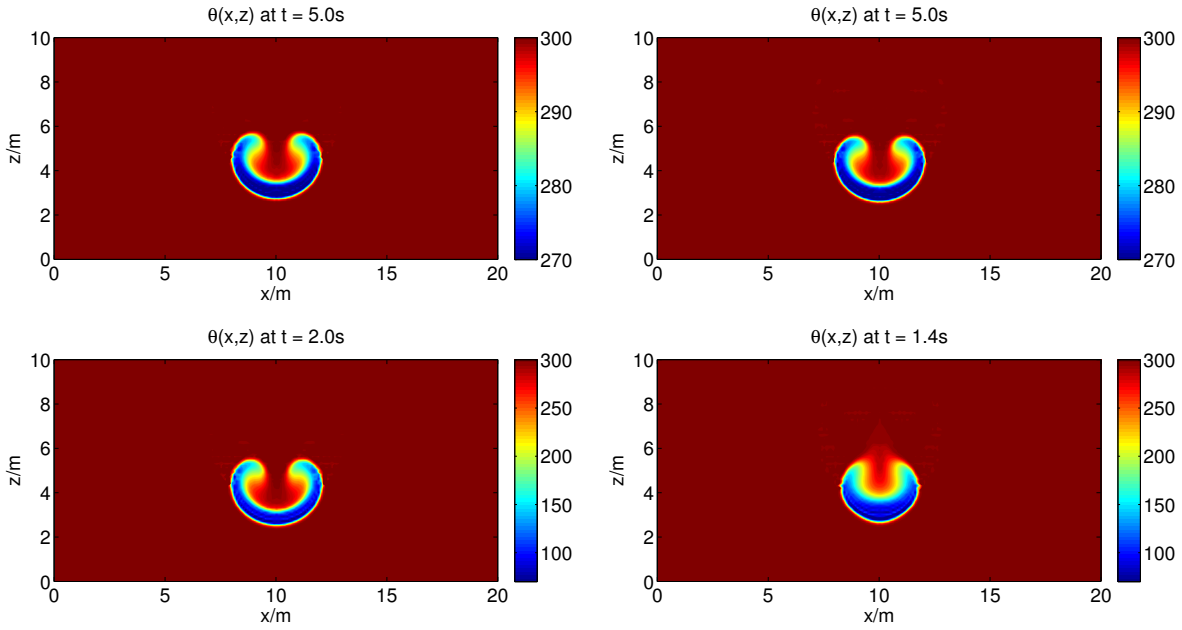

Figure 5.18: Potential temperature on regular meshes: comparison of results of the anelastic (left column) and pseudo-incompressible schemes (right column) for the falling cold air bubble; upper row: $\theta_{min}/\theta_{max} = 270\,\mathrm{K}/300\,\mathrm{K}$, lower row: $\theta_{min}/\theta_{max} = 90\,\mathrm{K}/300\,\mathrm{K}$.

The first baroclinic effect is prominent in both the anelastic and the pseudo-incompressible models. In the latter model, however, a second baroclinic effect counteracts the first one, in particular for large potential temperature variations (see lower right panel of Figure 5.18). Here, the nonlinear pressure gradient term causes a vorticity production proportional to $\nabla\theta \times \nabla\pi$. This effect is not captured by the anelastic (or Boussinesq) model as $\nabla \times \nabla(\bar{\theta}\pi) = 0$. With a maximum pressure value at the bottom of the droplet which decreases with height, and with an outward pointing potential temperature gradient, there develop hence in the pseudo-incompressible case positive vorticity on the right and negative vorticity on the left of the symmetry axis, counteracting the stretching. Therefore, in the upper right panel with a relative small potential temperature variation, the stretching is dominate, but in case of a larger variation (lower right panel) the second baroclinic effect counteracts the stretching.

In general, our variational schemes represent well the first, and in case of the pseudo-incompressible scheme also the second baroclinic effect for both mesh types. Our results agree well with those of [17] for low and for large potential temperature variations up to $\theta_{min}/\theta_{max} = 90\,\mathrm{K}/300\,\mathrm{K}$. As we do not apply flux limiters or any smoothing in our schemes (see also discussion in Section 5.3.1), we did not result in smooth solutions for the cold bubble test case with even higher potential temperature variations (as studied for instance by Klein [17]) when integrating the pseudo-incompressible scheme for more than 1.5 s. Here, too steep gradients in θ, which are strongly under-resolved on the front of the bubble, destroy the bubble's round shape. Moreover, this effect causes in both schemes, similarly to the warm bubble case, a decrease of the minimum θ value at the bubble's front of about 5 K for a variation of $\theta_{min}/\theta_{max} = 270\,\mathrm{K}/300\,\mathrm{K}$ and of about 20 K for $\theta_{min}/\theta_{max} = 90\,\mathrm{K}/300\,\mathrm{K}$.

Figure 5.19 shows, for regular meshes, the relative errors of total energy for the anelastic (left column) and pseudo-incompressible schemes for potential temperature profiles with $\delta\theta = 30\,\mathrm{K}$

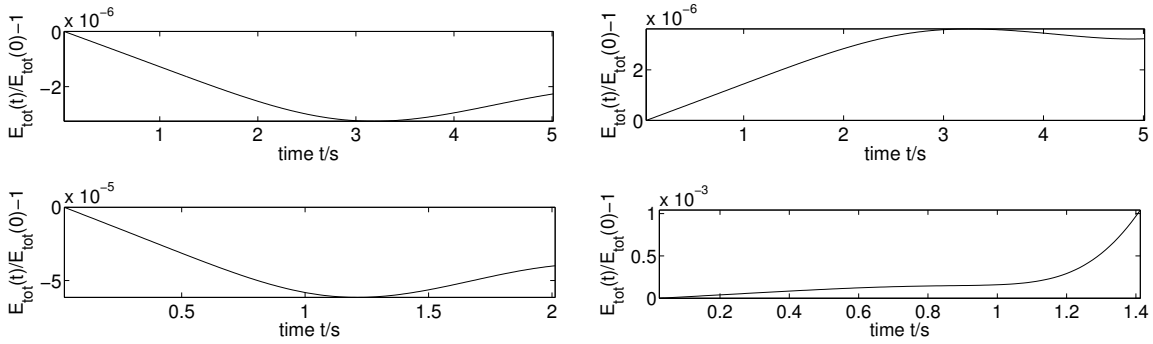

Figure 5.19: Relative error in total energy of the anelastic (left column) and pseudo-incompressible schemes (right column) for the falling cold air bubble; upper row: $\theta_{min}/\theta_{max} = 270\,\mathrm{K}/300\,\mathrm{K}$, lower row: $\theta_{min}/\theta_{max} = 90\,\mathrm{K}/300\,\mathrm{K}$.

(upper row) and $\delta\theta = 210\,\mathrm{K}$ (lower row). The values for total energy are well conserved while also here we realize for the pseudo-incompressible scheme a decrease in accuracy when the potential temperature gradients are too steep. For all cases, the values for mass, defined in equations (5.7) and (5.12), are very well conserved in the order of 10^{-14} (not shown). The relative errors obtain on irregular meshes are in the same order (also not shown).

6 Conclusion

In this paper we presented a summary of the variational discretization framework for soundproof (i.e. Boussinesq, anelastic, pseudo-incompressible) approximations of the Euler equations for perfect fluids, as introduced in [4]. This overview covers the variational derivation of the continuous as well as discrete equations of motion based on the Euler-Poincaré variational principles. In addition to [4], here we provided explicit vector-matrix formulations for these variational integrators and presented in detail the time discretization and the solving algorithm.

In addition, we provided a profound verification of these soundproof variational integrators for test cases of geophysical relevance, on both regular and irregular triangular C-grids. We considered a vertical slice model of the atmosphere and studied a hydrostatic adjustment process in which vertically varying reference states are in hydrostatic balance. When out of this equilibrium, the system tends to a balanced state by emitting internal gravity waves which are subject to a model-dependent dispersion relation. Numerical simulations showed that each of our variational integrators capture very well the characteristics of the corresponding dispersion relation, in particular the upper and lower bounds of permitted wave numbers.

Furthermore we verified that all schemes capture well the sensitive threshold of the Kelvin-Helmholtz instability (KHI), i.e for Richardson number J smaller then the critical value of 0.25, the flow structure develops in fact instabilities while it stays stably stratified otherwise. For to long integration times we obtain noisy solutions because in the versions presented we tested the pure variational integrators without dissipation.

To further test the nonlinear behavior, we performed advection dominated tests using a warm rising, resp., cold falling bubble in a cold, resp., warm environment. Our variational integrators perform very well when compared with reference literature, in particular they capture nicely the shape and advection speed of the bubbles. In all these cases studied, both mass

and energy are conserved to a high degree confirming the structure-preserving nature of our variational integrators.

In current and future work we derive and implement variational integrators for three dimensional soundproof models and we address the issue of noisy solutions by including dissipation in form of a variational or metriplectic approach associated to the developments in [14, 13, 11].

Acknowledgments

The authors thank D. Cugnet, M. Desbrun, F. Lott, and V. Zeitlin for helpful discussions and valuable feedback. Both authors were partially supported by the ANR project GEOMFLUID, ANR-14-CE23-0002-01. W. Bauer has received funding from the European Union's Horizon 2020 research and innovation programme under the Marie Skłodowska-Curie grant agreement No 657016.

References

[1] R. Abraham and J. E. Marsden, *Foundations of Mechanics*, Benjamin-Cummings Publ. Co., second edition, 1978.

[2] W. Bauer, M. Baumann, L. Scheck, A. Gassmann, V. Heuveline and S. C. Jones, Simulation of tropical-cyclone-like vortices in shallow-water icon-hex using goal-oriented r-adaptivity, *Theoretical and Computational Fluid Dynamics*, **28** (2014), 107–128.

[3] W. Bauer and F. Gay-Balmaz, Towards a geometric variational discretization of compressible fluids: the rotating shallow water equations, *J. Comp. Dyn.* **6**(1), 2019.

[4] W. Bauer and F. Gay-Balmaz, Variational integrators for anelastic and pseudo-incompressible flows, arXiv preprint arXiv:1701.06448, 2017.

[5] A. Bihlo and F. Valiquette, Symmetry-preserving numerical schemes, in *Symmetries and Integrability of Difference Equations*, Springer, 2017, 261–324.

[6] S. Blanes and F. Casas, *A Concise Introduction to Geometric Numerical Integration*, vol. 23, CRC Press, Boca Raton, 2016.

[7] M. Desbrun, E. S. Gawlik, F. Gay-Balmaz and V. Zeitlin, Variational discretization for rotating stratified fluids, *Discrete Continuous Dynam. Systems - A*, **34**(2014), 479–511.

[8] P. G. Drazin [1958], The stability of a shear layer in an unbounded heterogeneous inviscid fluid, *Journal of Fluid Mechanics*, **4**, 214–224.

[9] D. R. Durran, Improving the anelastic approximation, *J. Atmos. Sci*, **46** (1989), 1453–1461.

[10] D. R. Durran, *Numerical Methods for Wave Equations in Geophysical Fluid Dynamics*, second edition, Springer-Verlag, New York, 1999.

[11] C. Eldred and F. Gay-Balmaz, Single and double generator bracket formulations of geophysical fluids with irreversible processes, arXiv preprint arXiv:1811.11609, 2018.

[12] E. S. Gawlik, P. Mullen, D. Pavlov, J. E. Marsden and M. Desbrun, Geometric, variational discretization of continuum theories, *Physica D*, **240**(2011), 1724–1760.

[13] F. Gay-Balmaz, A variational derivation of the nonequilibrium thermodynamics of a moist atmosphere with rain process and its pseudoincompressible approximation, arXiv preprint arXiv:1701.03921, 2018.

[14] F. Gay-Balmaz and H. Yoshimura, A Lagrangian variational formalism for nonequilibrium thermodynamics. Part II: continuum systems, *J. Geom. Phys.*, **111**, 2017, 194–212.

[15] D. D. Holm, J. E. Marsden and T. S. Ratiu, The Euler-Poincaré equations and semidirect products with applications to continuum theories, *Adv. in Math.* **137** (1998), 1–81.

[16] E. Hairer, C. Lubich, and G. Wanner, *Geometric numerical integration: structure-preserving algorithms for ordinary differential equations*, Springer, Berlin, 2006.

[17] R. Klein, Asymptotics, structure, and integration of sound-proof atmospheric flow equations, *Theor. Comput. Fluid Dyn.*, **23** (2009), 161–195.

[18] H. Lamb, *Hydrodynamics*, Ch. 309, 310, Dover, 1932.

[19] B. Leimkuhler and S. Reich, *Simulating Hamiltonian dynamics*, Cambridge University Press, Cambridge, 2004.

[20] F. Lott [1989], Etudes des interactions entre une perturbation et un coulement moyen au voisinage d'un niveau critique: influence des dissipations, *Thèse de doctorat de l'Université Paris 6 (Ph.D.)*, 180pp.

[21] F. Lott and H. Teitelbaum [1992], Nonlinear dissipative critical level interaction in a stratified shear flow: instabilities and gravity waves, *Geophysical and Astrophysical Fluid Dynamics*, **66**, 133–167.

[22] F. Lipps and R. Hemler, A scale analysis of deep moist convection and some related numerical calculations, *J. Atmos. Sci.*, **29** (1982), 2192–2210.

[23] J. E. Marsden and T. S. Ratiu, *Introduction to Mechanics and Symmetry*, Texts in Applied Math., **17**, Springer-Verlag, 1994.

[24] J. E. Marsden and M. West, Discrete mechanics and variational integrators, *Acta Numer. 2001* **10** (2001), 357–514.

[25] Y. Ogura and N. Phillips, Scale analysis for deep and shallow convection in the atmosphere, *J. Atmos. Sci.*,**19** (1962), 173–179.

[26] D. Pavlov, P. Mullen, Y. Tong, E. Kanso, J. E. Marsden and M. Desbrun, Structure-preserving discretization of incompressible fluids, *Physica D*, **240**(2010), 443–458.

[27] J. M. Sanz-Serna and M. P. Calvo, *Numerical Hamiltonian problems*, vol. 7 of *Applied Mathematics and Mathematical Computation*, Chapman & Hall, London, 1994.

[28] A.T.S. Wan, A. Bihlo, and J.C. Nave, Conservative methods for dynamical systems, *SIAM J. Numer. Anal.* **55** (2017), 2255–2285.

[29] A.T.S. Wan and J.C. Nave., On the arbitrarily long-term stability of conservative methods, arXiv:1607.06160, 2016.

[30] R. Wilhelmson and Y. Ogura, The pressure perturbation and the numerical modeling of a cloud, *J. Atmos. Sci.*, **29** (1972), 1295–1307.